Astronomy & Astrophysics manuscript no. Perna14_sub
November 18, 2014
©ESO 2014

arXiv:1410.5468v2 [astro-ph.GA] 15 Nov 2014

Galaxy-wide outflows in z∼1.5 luminous obscured QSOs revealed through NIR slit-resolved spectroscopy

M. Perna[1,2⋆], M. Brusa[1,2,3⋆⋆], G. Cresci[4], A. Comastri[2], G. Lanzuisi[1,2], E. Lusso[4], A. Marconi[5], M. Salvato[3,6], G. Zamorani[2], A. Bongiorno,[9], V. Mainieri[7], R. Maiolino[8], and M. Mignoli[2]

[1] Dipartimento di Fisica e Astronomia, Università di Bologna, viale Berti Pichat 6/2, 40127 Bologna, Italy
[2] INAF - Osservatorio Astronomico di Bologna, via Ranzani 1, 40127 Bologna, Italy
[3] Max Planck Institut fur Extraterrestrische Physik, Giessenbachstrasse 1, 85748 Garching bei München, Germany
[4] INAF - Osservatorio Astrofisico di Arcetri, Largo Enrico Fermi 5, 50125 Firenze, Italy
[5] Dipartimento di Fisica e Astronomia, Università degli Studi di Firenze, via G.Sansone 1, 50019, Sesto Fiorentino (Firenze), Italy
[6] Excellence Cluster Universe, Boltzmannstrasse 2, D-85748 Garching bei München, Germany
[7] European Southern Observatory, Karl-Schwarzschild-str. 2, 85748 Garching bei München, Germany
[8] Cavendish Laboratory, University of Cambridge, 19 J. J. Thomson Ave., Cambridge CB3 0HE, UK
[9] INAF - Osservatorio Astronomico di Roma, via Frascati 33, 00044 Monte Porzio Catone (RM), Italy

Accepted 1988 December 15. Received 1988 December 14; in original form 1988 October 11

ABSTRACT

Aims. The co-evolution of galaxies and super massive black holes (SMBHs) requires that some sort of feedback mechanism is operating during the active galactic nuclei (AGN) phases. AGN driven winds are the most likely candidates for such feedback mechanism, but direct observational evidence of their existence and of their effects on the host galaxies are still scarce and their physical origin is still hotly debated.
Methods. X-shooter observations of a sample of X–ray selected, obscured quasars at z∼1.5, selected on the basis of their observed red colors and X–ray-to-optical flux ratio, have shown the presence of outflowing ionized gas identified by broad [OIII] emission lines in 6 out of 8 objects, confirming the efficiency of the selection criteria. Here we present slit-resolved spectroscopy for the two brightest sources, XID2028 and XID5321, to study the complex emission and absorption line kinematics.
Results. We detect outflow extended out to ∼ 10 kpc from the central black hole (BH), both as blueshifted and redshifted emission. Interestingly, we also detect kpc scale outflows in the [OII] emission lines and in the neutral gas component, traced by the sodium D and magnesium absorption lines, confirming that a substantial amount of the outflowing mass is in the form of neutral gas.
Conclusions. The measured gas velocities and the outflow kinetic powers, inferred under reasonable assumptions on the geometry and physical properties of these two systems, favor an AGN origin for the observed winds.

Key words. galaxies:active - galaxies: evolution - quasars:emission lines - quasars: individual:XID2028 - quasars: individual:XID5321

1. Introduction

Many of the most successful models of galaxy formation (e.g., Hopkins et al. 2006; King 2005) require energetic outflows, driven by active galactic nuclei (AGN), and extending over galaxy scales (i.e., ∼ 1-10 kpc) to reproduce the scaling relations observed in the local universe between host galaxies and black hole properties (e.g., Magorrian et al. 1998; Marconi & Hunt 2003; Ferrarese & Ford 2005; Kormendy & Ho 2013).

According to the most popular AGN-galaxies co-evolutionary models (e.g., Hopkins et al. 2006; Menci et al. 2008), the first phase of the quasi-stellar objects (QSOs) life is associated to rapid supermassive black hole (SMBH) growth and efficient star formation (SF) in a dust-enshrouded, dense environment: in this phase AGN are dust and gas obscured. This is followed by the "blow-out" or "feedback" phase during which the SMBH releases radiative and kinetic energy in the form of powerful, outflowing wind, before becoming a "normal" unobscured QSO once the obscuring material has been cleared out (see, e.g., Hopkins et al. 2008). In this framework, AGN feedback should be revealed through the presence of outflowing material driven by energetic winds (see, e.g., Fabian 2012; Zubovas & King 2012). However, these outflows could also be powered by SF activity (e.g., Heckman, Armus & Miley 1990; Veilleux, Cecil & Bland-Hawthorn 2005) and it is not fully understood the relative dominance of the two different mechanisms involved. Regardless of their nature, during the peak of star formation (z∼ 1.5-3) outflows are believed to play a pivotal role in shaping galaxies, because they regulate both SF and black hole growth.

The SF- and AGN-induced outflows have recently been found at low-z, involving outflowing mass in the form of molecular gas (e.g., Feruglio et al. 2010; Sturm et al. 2011; Cicone et al. 2012, 2014), neutral (e.g., Rupke & Veilleux 2011, 2013), and ionized gas (e.g., Westmoquette et al. 2012; Rupke & Veilleux 2013; Rodríguez-Zaurín et al. 2013; Harrison et al. 2012), as well as at high-z, in QSOs (Maiolino et al. 2012; Harrison et al. 2012; Cano-Díaz et al. 2012) and in massive SF galaxies (Föerster-Schreiber et al. 2014; Genzel et al. 2014). The Sloan digital sky survey (SDSS) enabled the selection of

⋆ E-mail: michele.perna4@unibo.it
⋆⋆ E-mail: marcella.brusa3@unibo.it

candidate sources hosings outflows at z< 0.5 on the basis of well-defined spectral signatures, such as broad FWHM in the [OIII]$\lambda\lambda$4959,5007 lines and/or double peaked profiles that can be ascribed to complex underlying kinematics (e.g., Liu et al. 2010; Fu et al. 2012). In most cases, the targets have been followed-up with integral field unit (IFU) instruments to assess the existence and the real extension of the outflows (e.g., Greene et al. 2012; Harrison et al. 2014). In recent years, this detailed study has also been extended to higher redshifts (z> 1) with spatially resolved spectroscopy with high resolution spectrograph and/or near infrared IFU instruments (see, e.g., Harrison et al. 2012). However, most of the results at high-z are still based on the observations of very luminous, unobscured QSOs, in which the blow-out phase is expected to be near its end, or in galaxies with unusually high star formation rate (SFR; e.g., submillimeter galaxies, SMGs) for which the contribution of SF winds in sustaining the outflow cannot be completely excluded (e.g., Harrison et al. 2012).

Given that the critical coalescence/blow-out phase is expected to be very short (<< 500 Myr; see, e.g., Menci et al. 2008), obscured and X–ray active (e.g., accretion on the BH is close to its maximum), the crucial point to study the feedback effects on the host galaxies is to select such objects as close as possible at the maximum of this phase. Large area X–ray surveys with the associated high-quality multiwavelength data provide the necessary tool for selecting these very rare sources. Luminous X–ray selected obscured AGN represent optimal targets for the search of objects where AGN feedback is expected to halt SF and to start "cleaning" out gas from the galaxy. In a previous work (Brusa et al. 2010, hereinafter B10) based on XMM-Newton observations of the COSMOS field (Hasinger et al. 2007; Cappelluti et al. 2009), we proposed a criterion for isolating the objects in the "feedback" phase on the basis of their observed red colors and high X–ray-to-optical and/or mid-infrared-to-optical flux ratios. A dedicated X-shooter campaign on a small subsample of such luminous sources at z$\sim$ 1.5 has convincingly shown that the proposed selection criteria are robust: the presence of outflowing material with velocities up to 1500 km s^{-1} was indeed detected in six out of eight sources, confirming the efficiency of the selection in isolating such rare objects (Brusa et al. 2014, B14).

Here we present a more in-depth study of the two brightest sources, XID2028 at z= 1.5927 and XID5321 at z= 1.4702, aimed at studying in more details the properties of the outflowing [OIII] ionized gas unveiled by B14, through slit-resolved spectroscopy, i.e. to map and locate the outflowing components outside of the central slit and determine its energetics. In addition, we show the presence of outflows also in the [OII]$\lambda\lambda$3726,3729 emission and, more interestingly, in the sodium (NaD$\lambda\lambda$5890,5896) and magnesium (MgII$\lambda\lambda$2796,2803 and MgIλ2853) absorption lines in both sources, corresponding to a neutral phase of the outflow. The paper is organized as follows. Section 2 presents the target properties; Section 3 presents the X-shooter data analysis and the results of the spectral fitting; Section 4 discusses additional proofs of outflowing material, investigating the presence of shifted components in the detected (MgII, MgI, and NaD) absorption and ([OII]) emission lines; Section 5 shows evidence of the AGN photoionization origin of the emission lines through rest-frame optical diagnostics; Section 6 discusses the energetic output associated to the outflow. Finally, Section 7 summarizes the main results and their implications. All the rest frame wavelengths are given in the air, as quoted in http://www.sdss3.org/dr8/spectro/spectra.php. Throughout the paper, we adopt the cosmological parameters H_0 = 70 km s^{-1} Mpc^{-1}, Ω_m=0.3 and Ω_Λ=0.7 (Sperger et al. 2003).

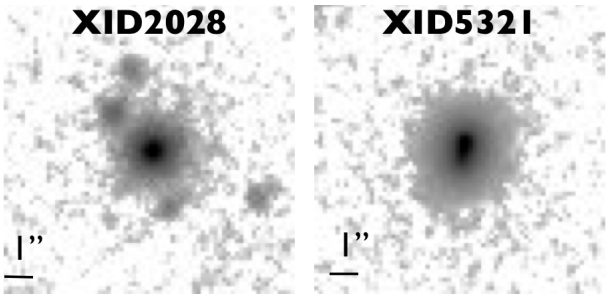

Fig. 1: Cosmos CFHT/WIRCam H band images (10"x10") of XID2028 (left) and XID5321 (right). Images are oriented with north up and east to the left.

2. Target properties

We have completed an X-shooter near-infrared spectroscopy campaign on a sample of ten luminous X–ray selected obscured QSOs at z$\sim$ 1.5 from the XMM-COSMOS survey (B14). The targets were selected on the basis of their observed red colors and high X–ray-to-optical and/or mid-infrared-to-optical flux ratio (B10). Complete details about the target selection, the X-shooter observations, and data reduction are given in B14. Briefly, we recall here that all the sources for which the presence of outflowing gas has been detected share the following common properties: they are luminous AGN (with $L_{bol} \sim 10^{45-46.5}$ erg s^{-1}), X–ray absorbed ($N_H \sim 10^{21-23}$ cm^{-2}) and they are hosted in massive galaxies, with stellar masses $M_* = 10^{11-12}$ M$_\odot$.

The two brightest X–ray targets, XID2028 and XID5321, with unabsorbed luminosity $log(L_X) > 45$ erg s^{-1} in the 2-10 keV, are those detected at the highest S/N in the X-shooter NIR spectrum. These two sources are also extreme in the host galaxies properties: they have stellar masses on the order of 10^{12} M$_\odot$ and exhibit substantial SFRs (SFR$\sim$250 M$_\odot$/yr, assuming a Chabrier IMF; see B14) as inferred from the Herschel PACS detection after a detailed spectral energy distribution (SED) fitting decomposition (B14, Bongiorno et al. 2014; see also below). The SFR observed in XID2028 and XID5321 are consistent with those observed for the normal population of star forming galaxies at those redshifts and place the targets on the main sequence (Whitaker et al. 2012; Rodighiero et al. 2011; see also B14). Finally, they have BH masses on the order of 10^{9-10} $M_\odot$, obtained as Hα single-epoch virial estimates (Bongiorno et al. 2014). The Hβ BLR emission lines are considerably extincted (see B14; Section 5.1), making these sources consistent with a type 1.8 nature.

The radio flux measured at 1.4 GHz (observer frame) in the Very Large Array (VLA) observations of the COSMOS field (Schinnerer et al. 2010) are 102±20μJy and 180±24μJy for XID2028 and XID5321, respectively. Assuming $S_\nu \propto \nu^{-0.7}$, the radio luminosities are $L_{1.4GHz}(5321) = 4.7 \cdot 10^{24}$ W Hz^{-1} and $L_{1.4GHz}(2028) = 3.3 \cdot 10^{24}$ W Hz^{-1}, corresponding to low ratios between the far-infrared and radio emission ($q_{IR} \sim 0.8$; Ivison et al. 2010); these values place the targets in the radio quiet class (see, e.g., Bonzini et al. 2013), guaranteeing marginal contribution from radio jets in the energetic of the systems.

Figure 1 shows the CFHT/WIRCam cutouts of the H band image of the two targets. While for XID2028 we can firmly exclude the presence of two sources within 0.9" (i.e., the size of our slit; see below) given the high resolution HST/ACS data

available (see Figure 4 left, upper panel; see also B10, B14 and Cresci et al. 2014), the presence of two sources in XID5321, not resolved in our imaging data (for this source we lack ACS coverage), cannot be excluded. We will discuss this in more details in Section 7.

2.1. SED fitting

The selected XMM-COSMOS sources benefit from a rich multi-wavelength data-set with *complete* and *homogenized* ultraviolet to far-infrared (including Herschel data) to radio coverage, and extensive spectroscopic follow–up. More details on the photometry collected for the counterparts of XMM-COSMOS can be found in B10, with the addition of the PACS datapoints (Lutz et al. 2011). The rest-frame SEDs of the two targets, previously presented in Lusso et al. (2012), were reanalyzed using the SED-fitting code presented in Lusso et al. (2013) (see below for details), and are shown in Figure 2. In addition to the longer wavelength data, in each panel of Figure 2 we also plot the X–ray datapoints in the soft and hard energy bands (black points at log $\nu \sim 18$).

In obscured AGN the optical-UV nuclear emission is absorbed by the dusty torus and reprocessed in the IR. Therefore the average SED is characterized by an optical-UV luminosity much lower than that seen in unobscured AGN (e.g., the big blue bump (BBB), Elvis et al. 1994) and partly due to the host galaxy. The contribution of the AGN is maximum at MIR wavelengths (around 12 μm, Gandhi et al. 2009), while most of the emission at longer wavelengths can be ascribed to star formation only. The data points from far-infrared to the UV band have therefore been fit with a combination of four components: 1) a stellar component to account for the host galaxy contribution (green curves); 2) a torus component to account for the reprocessed AGN emission in the MIR (brown curves); 3) a BBB component to account for the AGN accretion disk thermal emission (blue curves); 4) a starburst component to account for the on-going star formation (grey curves). The red lines represent the best fit SEDs. We notice that, given the quality of the data points (e.g., dense sampling, bright fluxes and small errors) and the distinctive shape of the SEDs, the decomposition in the different components is basically independent from the details of the fitting code, both in terms of templates used, and minimization procedure. In particular, we verified that all the physical parameters of interest (e.g., AGN luminosities, SFR, extinction) are solid and do vary only marginally (within 10-20%) when other SED fitting codes developed in COSMOS are used instead (e.g., Bongiorno et al. 2012; Delvecchio et al. 2014). The only parameter which vary significantly (a factor of 2) is the stellar mass, contingent on the presence of the reddened BBB component in these targets. From these fits we infer reddening values E(B-V)=0.95 and 1.0 for the AGN components in XID5321 and XID2028, respectively. The extinctions are obtained by reddening the BBB template according to the Small Magellanic Clouds (SMC) law (Prevot et al. 1984). Overall, the AGN contribution to the bolometric output (in the range 1-1000 μm) is $\sim$ 60% for XID2028 and $\sim$ 80% for XID5321.Accounting for the extinctions, we infer total bolometric luminosities of $L_{bol} \sim 2 \times 10^{46}$ erg s^{-1}. Using the BH masses already mentioned, we obtain Eddington ratios of $L_{bol}/L_{Edd} \sim 0.01 - 0.05$ (see B14).

Composite SEDs for a sample of Type 2 AGN in XMM-COSMOS are presented in Lusso et al. (2011) for different bins of redshifts and luminosities. In each panel of Figure 2 we have plotted the composite SED constructed in a similar range of luminosity of our targets (log $L_{8\mu m} \sim 44.3 - 45.7$, which roughly corresponds to log $L_{\rm bol} \sim 45.3 - 46.7$). From the comparison of the SED of our targets and the average SED of X–ray selected sources at the same luminosity, we note that the X–ray datapoints of XID2028 and XID5321 are above the average SED by $\sim$ 0.5 dex. This confirms that these 2 targets are X–ray loud (as per their selection on the basis of the high X/O ratio) but optically weak (without a clear view of the accretion disc emission). Indeed, the flat shape between 1-10 μm and the presence of BLR lines in the NIR X-shooter spectra, are all consistent with a transition from type 2 to type 1 through a reddened type 1 phase.

Table 1: Observations log

XID	start date	Seeing [a]	expo	P.A.
2028	2013-02-09	0.92	3600	90
	2013-02-09		3378	
	2008-01-08[b]	1	9600	
5321	2013-02-10	0.74	3600	135
	2013-02-10		3378	

[a] Delivered seeing corrected by airmass
[b] Keck/DEIMOS

2.2. X–ray spectra

For both sources medium-deep X–ray spectra are available from the XMM-COSMOS survey (Mainieri et al. 2011). X–ray spectra were extracted using standard techniques and calibration files, following the procedures described in details in Mainieri et al. (2011) and Lanzuisi et al. (2014).The counts from the same camera (MOS, pn) are merged together, and the responses are created for each camera. The total number of net counts used in the spectral fitting sums up to $\sim$ 1500 for both sources.

The joint fit to the pn and MOS XMM spectra are presented in Figure 3 (left panel). An absorbed power law provides a good fit over the $\sim$ 0.3–8 keV energy range. For both sources the best fit intrinsic slope and absorption column density are similar: $\Gamma \simeq 1.84 \pm 0.12$, $N_H \sim 7.1 \pm 0.2 \times 10^{21}$ cm^{-2} for XID2028, and $\Gamma \simeq 1.78 \pm 0.12$, $N_H \sim 5.8 \pm 0.2 \times 10^{21}$ cm^{-2} for XID5321. The N_H versus Γ confidence contours (68, 90 and 99%) are shown in Figure 3 (right panels). There is no evidence of iron Kα emission with 90% upper limits of 100 eV and 250 eV (rest–frame) in XID2028 and XID5321, respectively. The addition of a Compton reflection component subtending a 2π angle at the continuum source marginally improves the fits ($\Delta\chi^2 \sim 2$). The intrinsic spectral slope gets steeper $\Gamma \sim 1.93$–1.99 and the intrinsic absorption higher $N_H \sim 7$–8×10^{21} cm^{-2} respectively. The moderate, but significant intrinsic X–ray absorption argues against a pure Type 1 nature, while it is fully consistent with the Type 1.8 classification obtained by the near infrared X-shooter spectrum. The moderate obscuration observed in the X–rays coupled with the Eddington ratio ($\lambda_{\rm Edd} \sim 1-5\%$) places these objects in the region of "shortlived clouds" presented in Raimundo et al. (2010), where outflows or transient absorption are expected to happen. The optical reddening is fully consistent with the cold gas absorption measured in X–rays for a Galactic dust to gas ratio (Maiolino et al. 2001). [1] The observed intrinsic absorption could therefore be

[1] N_H determines to which wavelengths the medium is opaque and to which wavelengths the medium is transparent, where a medium with $N_H > 10^{21} cm^{-2}$ will obscure the UV emission, a medium with $N_H > 10^{22}$ will obscure the broad Hα line and the 3 μm emission, and a medium with $N_H > 10^{23}$ will obscure the 10 μm emission. All the numbers assume a Galactic dust composition and dust to gas ratio.

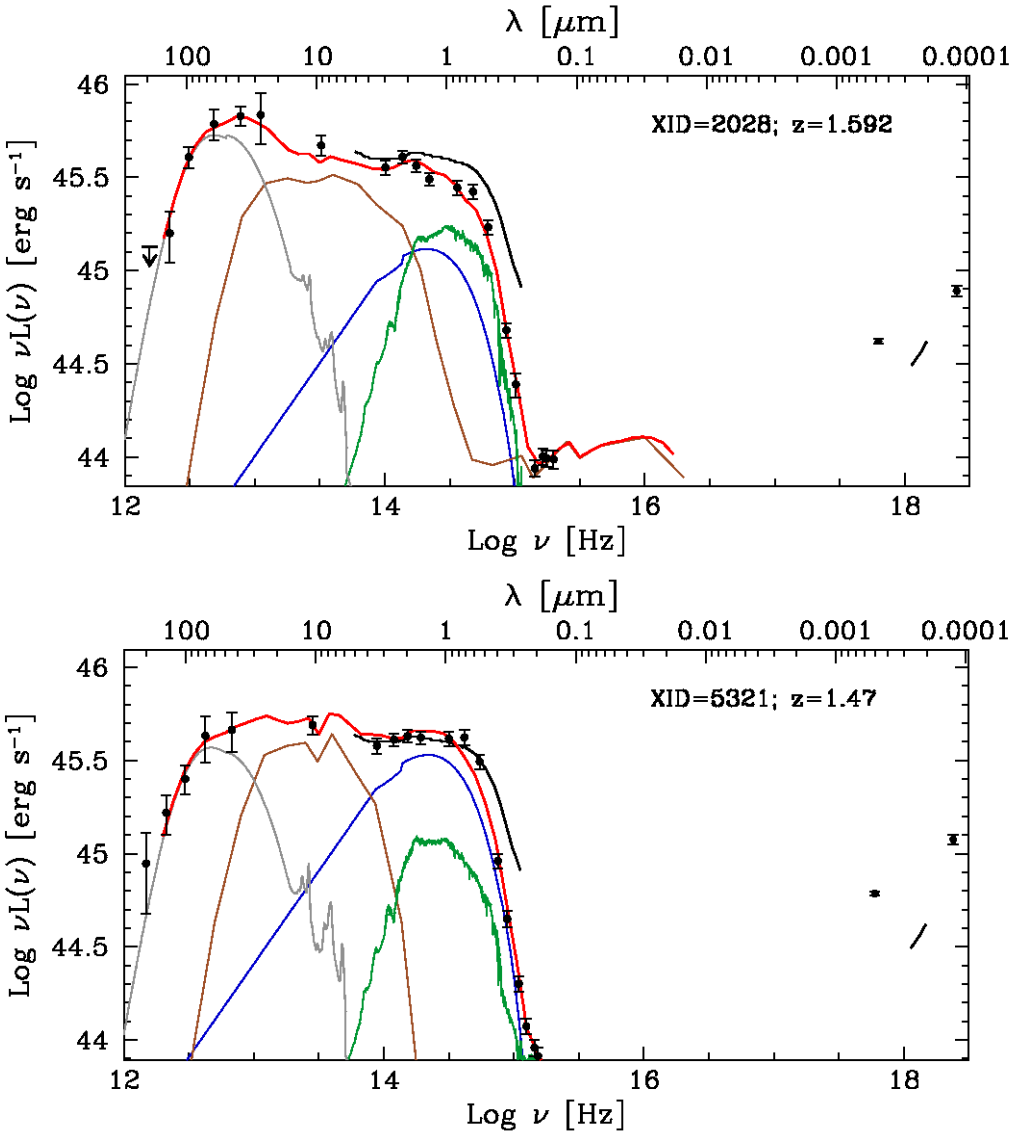

Fig. 2: SED fits of XID2028 and XID5321. Black circles are the observed photometry data. The grey, brown, blue and green lines correspond to the starburst, AGN torus and disk, and host-galaxy templates found as best fit solutions. The red lines represent the best fit SEDs. The black lines represent the mean SED computed by Lusso et al. (2011) for obscured AGN in the XMM-COSMOS survey at redshift z= 1.5 and with similar bolometric luminosity.

consistent with material in the host galaxy, or with some circumnuclear material such as a low column density torus or the outer parts of a thicker one.

3. NIR slit-resolved spectroscopy analysis

XID2028 and XID5321 have been observed with the X-shooter spectrograph (Dodorico et al. 2006; Vernet et al. 2011) on the ESO VLT-UT2 (Kueyen) during the nights of February 8-10, 2013 (ID: 092A.0830, PI: Brusa). As presented in B14, we revealed the presence of outflowing components associated to the most prominent Narrow Line Region (NLR) emission lines in the Hβ-[OIII] and Hα-NII regions, with velocity shifts V_S with respect to the systemic features, on the order of $|V_S| \sim 350$ - 450 km s^{-1}, in the nuclear spectra of both sources on an aperture of $\sim 1''$. XID2028 shows a blueshifted component, while XID5321 shows a less common redshifted component (see also Villar-Martín et al. 2011, Harrison et al. 2012, Bae & Woo 2014 for other examples of [OIII] lines with redshifted broad wings).

Here we analyze in more detail the X-shooter spectra of the two sources, with the aim of determining more accurate estimates of the key parameters (spatial extension, outflow velocity and flux) related to the outflowing winds.

3.1. Spatial extension

The analysis presented here is based on spectra extracted from three different spatial regions (*a*, *b*, *c*) of each system along the slit (see Figure 4). For each source, the (*b*) region is centered on the nucleus as determined from the peak of the spatial profile of the continuum emission (see below), and covers a projected region of 0.85x0.90", i.e. ~ 7.3 x 7.7 kpc. The (*a*) and (*c*) apertures, instead, cover the same projected regions in size, but are extracted from two regions offset from the nucleus. The slit po-

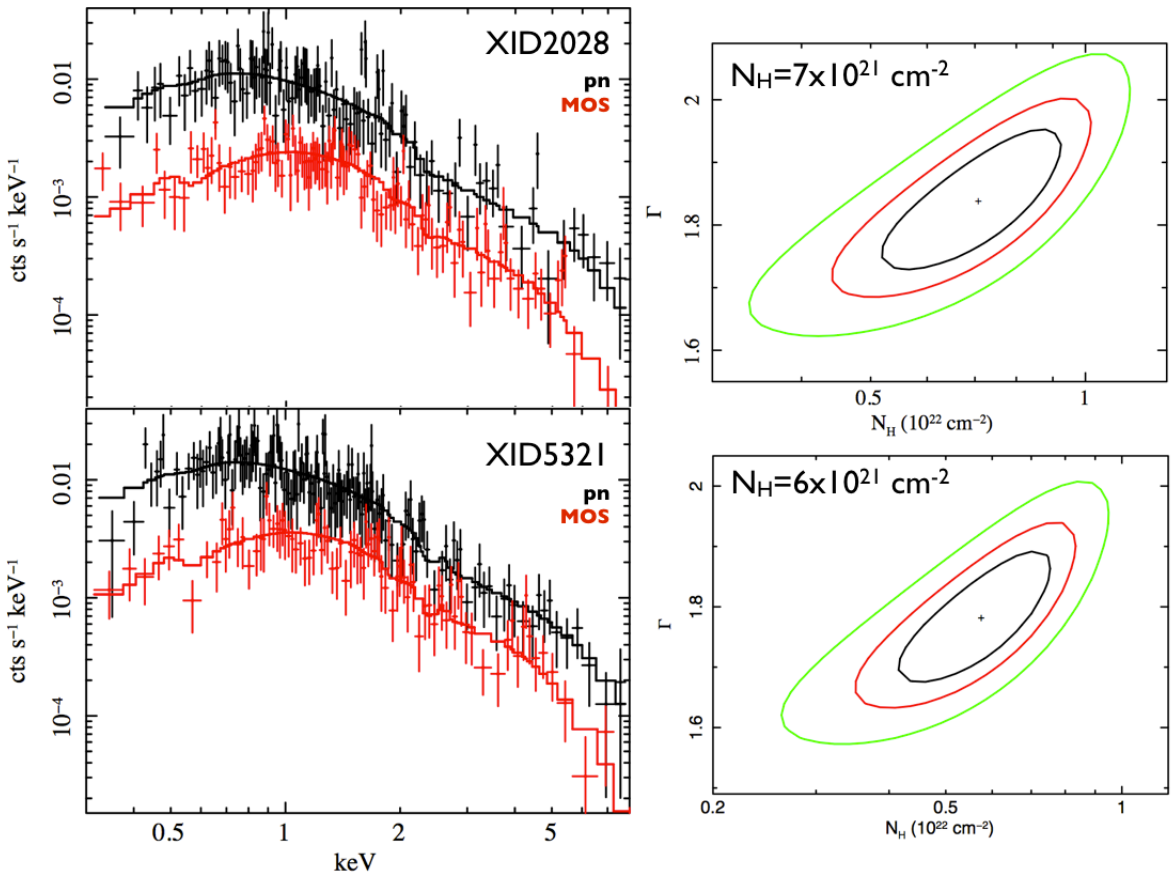

Fig. 3: X–ray spectra of XID2028 (top, left) and XID5321 (bottom, left). The different datasets used (XMM pn and MOS), are labeled in different colors. The best fit model is also shown as a solid line for each dataset. On the right are shown the combined constraints on N_H and the spectral slope, with confidence contours at 68, 95 and 99% level.

sition of the sources and the spatial location of each aperture are shown in the upper panels of Figure 4.

The spatial profiles along the slit of the 2D spectra are shown in Figure 4 (bottom panels). The dotted lines demark the regions indicating the location of the three apertures described above, as labeled. The *solid curves* show the spatial profile of the continuum flux, obtained by averaging profiles extracted at many line-free regions along the entire dispersion axis; the *dashed curves* show the spatial profile of the emission in the [OIII]λ5007 line. For XID2028, the different profiles of the solid and dashed curves represent the first evidence that complex narrow line kinematics is in place. The small displacement between the spatial profiles of XID5321 is instead due to a slight tilt along the dispersion axis. Hence, a possible error in the determination of the peak of the spatial profile of the continuum flux, and therefore of the location of the nuclear region of XID5321, could be present. However, it does not significantly change the results in the following analysis, given that 1 pixel gaps between the three regions are present.

Figure 5 shows the spectra extracted from each region, indicated with letters (a, b, c), centered on [OIII]λ5007. In the figure, solid lines represent the fits that best reproduce the line profiles; details are given in the next Sections. For both sources, significant signal is detected only in one off-nuclear aperture (aperture (a) for XID2028, (c) for XID5321). We note that seeing conditions were $\sim$ 0.8", hence the extension seen ($\gtrsim 2 \times$ seeing) is fully resolved and is not due to seeing effects. Figure 5 shows that complex multicomponent profiles in the [OIII]λ5007 line are detected not only in the nuclear region (covering up to 4-5 kpc, see B14), but out to a distance of R $\approx$ 10-12 kpc, therefore extending considerably over the host galaxy. SINFONI observations of XID2028 (Cresci et al. 2014) confirm that extended [OIII] emission, roughly orientated along our X-Shooter slit, is extending up to 13 kpc from the nucleus. We therefore assume that the outflow in each source extends out to $\approx$ 11 kpc from the central black hole.

3.2. Velocities and fluxes

To determine the dynamics and the outflow properties, we proceed using two approaches: a simultaneous line fitting and a non-parametric analysis. The two approaches are justified by the fact that with the simultaneous line fitting we can have a better estimate of the unperturbed and outflowing gas fluxes separately, while with the non-parametric analysis we can infer more accurate outflow velocity measurements. In both cases, the spectra were shifted to the rest frame using the redshift found by B14 and the continuum flux in the vicinity of emission lines was fit with a power-law model.

3.2.1. Simultaneous modeling the Hβ + [OIII] and Hα + [NII] line complexes

The first approach is the one described in B14, applied to three different apertures along the slit. In this case, to derive the outflow properties we used the constraints in accor-

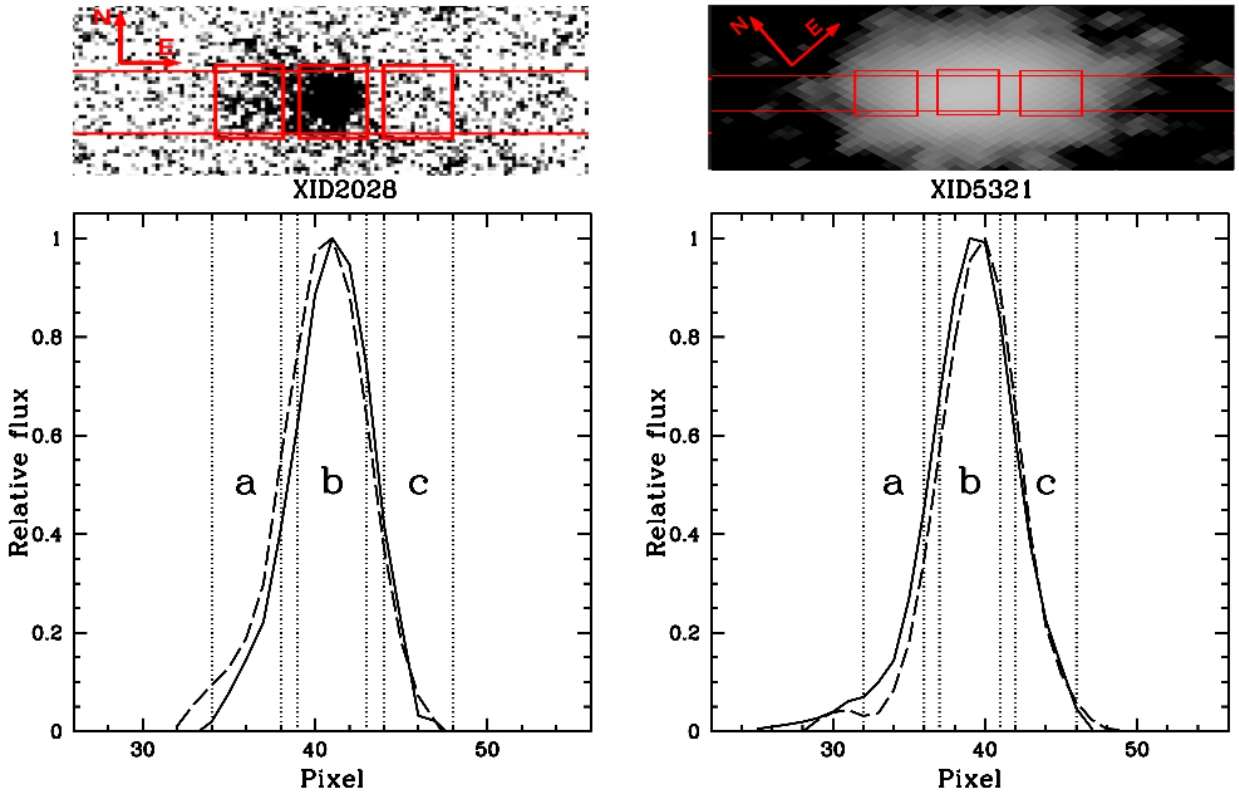

Fig. 4: (*lower panels*) Spatial profiles of the 2D spectrum of XID2028 (left) and XID5321 (right) of the continuum flux (solid curves) and in the proximity of [OIII]λ5007 emission line (long dashed curves). Both continuum and [OIII]λ5007 wavelength range profiles are normalized to unity. The dotted lines shows the demarcations of the three regions from which the apertures were extracted (denoted with *a*, *b*, and *c*). (*upper panels*) HST/ACS F814 image of XID2028 (left) and J-band UltraVista image of XID5321 (right) showing the position and orientation of the 0.9" slit and the spatial locations of the three apertures.

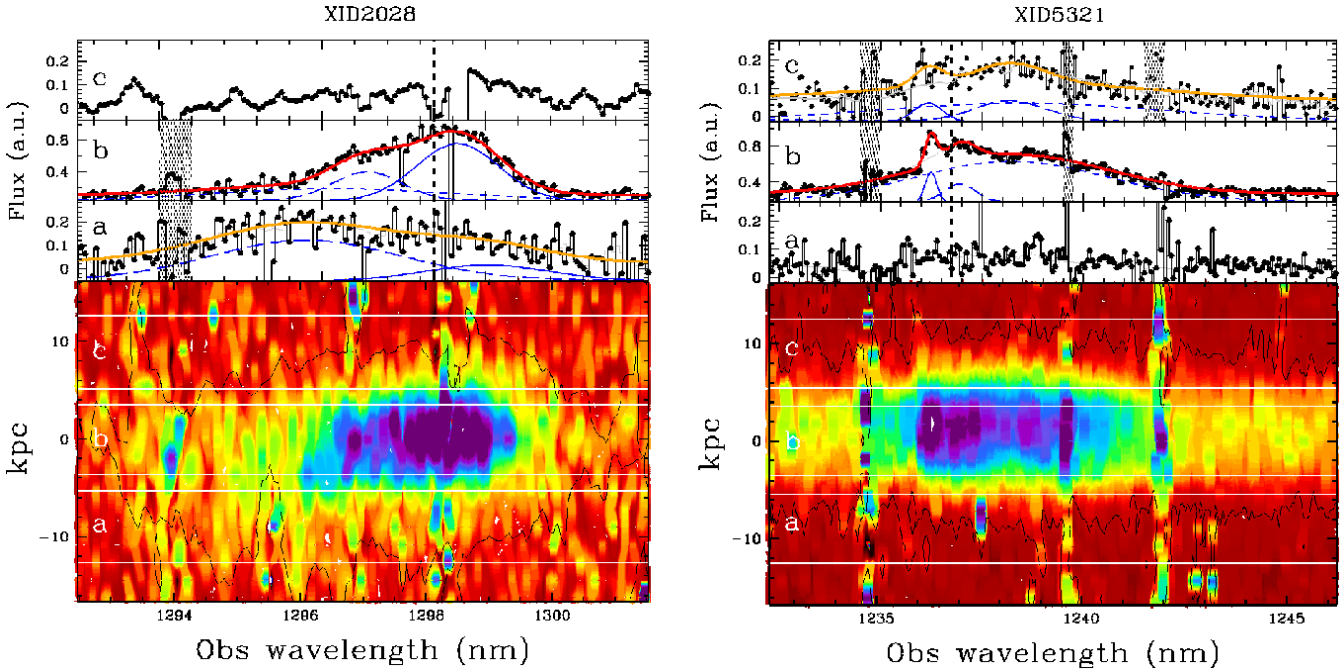

Fig. 5: XID2028 (left) and XID5321 (right) X-Shooter spectra of the regions *a*, *b*, *c*, centered on [OIII]λ5007. The red and orange lines indicate the best fit solutions that reproduce the line profiles according to the non-parametric approach (see Section 3.2.2). The Gaussian components are shown with arbitrary normalization in order to ease the visualization. The dotted lines mark the wavelength of [OIII]λ5007 at the systemic redshift determined by B14. The lower panels show the 2D spectra, indicating the apertures used to extract the 1D spectra seen in the upper panels. Red to blue colors represent increasing flux. Extended vertical structures, like the one at $\sim$ 1242 nm (right), delineate strong sky features and are indicated in the 1D spectra as shaded areas.

dance with atomic physics (i.e., doublet flux ratios, wavelength separations; for more details see B14). Briefly, we fit simultaneously the two regions (Hβ+ [OIII] and Hα+ [NII]$\lambda\lambda$6548,6583+[SII]$\lambda\lambda$6716,6731) with three sets of Gaussian profiles in the nuclear apertures: two sets of narrow Gaussian lines, with FWHM $\lesssim$ 500 km s^{-1} and FWHM $\gtrsim$ 500 km s^{-1} respectively, for each detectable emission line, and a broad (FWHM > 2000 km s^{-1}) Gaussian or Lorentzian line to account for the presence of the Hα and Hβ emission originated in the BLR. In the off-nuclear apertures, where we do not expect to see BLR emission lines, and the S/N is lower, only one set of Gaussian profiles is used, with no limit to the FWHM.

Figure 6 shows the best fit solution of our spectra, as in Fig. 6 of B14, for the apertures *a* and *b* for XID2028 and *b* and *c* for XID5321. It turns out, especially for the [OIII] emission lines, that the profiles of the nuclear regions (red curves in the figure) are broad and asymmetric. We do not see the same effect for the other lines, Hα, Hβ and the forbidden [NII] and [SII], because they are blended with the BLR component and/or of lower S/N.

Using all the constraints due to the atomic physics, and therefore minimizing the degeneracy (especially in the [NII]+Hα profile), this approach allows us to show, in the nuclear regions, the presence of one component associated with overall narrow profiles (FWHM ∼ 300-500 km s^{-1}), likely associated with the systemic NLR, and of another component with FWHM ∼ 1300-1600 km s^{-1} and shifted with respect to the narrower (V_S ∼ 340 km s^{-1}), associated to outflowing emitting gas. Moreover, it allows us to study the physical conditions of the ionizing gas of these two components using the line flux ratios (see Section 5). The profiles in the off-nuclear regions (orange curves in Figure 6) appear broader and shifted with respect to those determined in the nuclear regions (see Section 3.3), and are likely associated to outflowing emitting gas.

In the following, we will refer to the "outflow" components as the Gaussian profiles with FWHM $\gg$ 500 km s^{-1} of the best fit solution of this approach, not to be confused with the systemic narrow (FWHM $\lesssim$ 500 km s^{-1}) profiles, likely associated to the NLR.

3.2.2. Non-parametric analysis

We used the non-parametric analysis for the only [OIII]λ5007 emission line. Non-parametric measures do not depend strongly on the specific fitting procedure and on the physical interpretation of any of the parameters of the individual Gaussian profile, pointing to obtain a noiseless approximation to the emission line profile. Hence, once a local continuum was subtracted, we fit the [OIII] with as many Gaussian profiles as needed (3 at most) in order to reproduce the overall shape of the line profile.

The best fit solutions are shown in Figure 5 for the different apertures along the slits. Gaussian components with widths up to ∼ 1000 km s^{-1} are required, especially in the off-nuclear apertures. In particular, the [OIII] line of the nuclear aperture of XID5321 presents a peculiar profile, with different peaks. Two out of the three Gaussian lines that reproduce the total profile have width smaller than 500 km s^{-1}, and could be attributed to the NLR and star forming regions. Alternatively, they can be originating in two distinct systems (e.g., merging galaxies) not resolved by our imaging data.

Once the profile has been accurately reproduced, we used non-parametric measurements of the [OIII] emission line profiles (e.g., Zakamska & Greene 2014; Liu et al. 2013; Rupke & Veilleux 2013) carried out by measuring velocity v at which a given fraction of the line flux is collected, using the cumulative flux function $F(v) = \int_{-\infty}^{v} F_v(v')\,dv'$. The position of $v = 0$ of the cumulative flux is determined using the systemic redshift found by B14. Using the best fit solutions and following the prescription indicated by Zakamska & Greene (2014), we estimated for the total [OIII] profiles the following parameters:

(i) The line width $w80$, the width comprising 80% of the flux, that for a Gaussian profile is very close to the FWHM value. It is defined as the difference between the velocity at 90% ($v90$) and 10% ($v10$) of the cumulative flux, respectively;

(ii) The velocity offset of the broad underlying wings, ΔV, measured as ($v05$ + $v95$)/2, with $v95$ and $v05$ defined as above;

(iii) A maximum velocity parameter v_{max}, defined as $v02$ when blue prominent broad wings are present, or as $v98$ when red ones are, on the contrary, present.

In contrast to v_{max}, values of $w80$ and ΔV include only differences between velocities and do not depend on the accurate determination of the systemic velocity. A possible residual error in the determination of the systemic velocity, however, may produce a variation of at most few tens of km s^{-1} in the v_{max} value, corresponding to variation of a few % (see below). Figure 7 shows the comparison between [OIII] velocity profiles for the nuclear (upper panels, red curves) and the off-nuclear regions (lower panels), with the non-parametric measurements of the best fit labeled. The profiles in the lateral apertures appear broad and shifted with respect to the systemic velocity determined in the nuclear regions, thus confirming the spatial extent of the outflows. In particular, v_{max} increases by ∼ 200 km s^{-1} going from the nuclear to the off-nuclear apertures, for both sources. The [OIII]λ5007 of XID5321 shows, in both apertures, also a blueshifted wing, although it is much less extended than the red wing.

We stress here that the use of a larger sets of Gaussian profiles permits a better approximation to the emission line profile and more accurate velocity measurements, but increases the degeneracy between the Gaussian components, and thus does not allow a flux estimation for the NLR and outflowing emitting gas separately, in contrast to the simultaneous fit approach. Thus both approaches are crucial for our analysis.

3.3. Results

We fit the Gaussian profiles using a fortran code implementing the Minuit package (James & Roos 1975). In order to estimate errors associated to our measurements, we used Monte Carlo simulations. For each fit parameters, we collected 1000 mock spectra using the best-fit final models (red and orange curves in Figure 5 and 6), added Gaussian random noise (based on the standard deviation of the corresponding local continuum), and fit them. The errors were calculated by taking the range that contains 68.3% of values evaluated from the obtained distributions for each component/ non-parametric measurement. We also note that since line profiles are non-Gaussian and much broader than the spectral resolution (see Section 4.2), we did not correct the observed profiles for instrumental effects and report all values as measured.

In Table 2 we quote the v_{max}, the line widths $w80$ and the velocity shifts ΔV as obtained from the non-parametric analysis, and the FWHM of the outflow components and the velocity shift V_S from the simultaneous fitting, all values which are used as estimator of velocity of the outflow in the literature (e.g.,

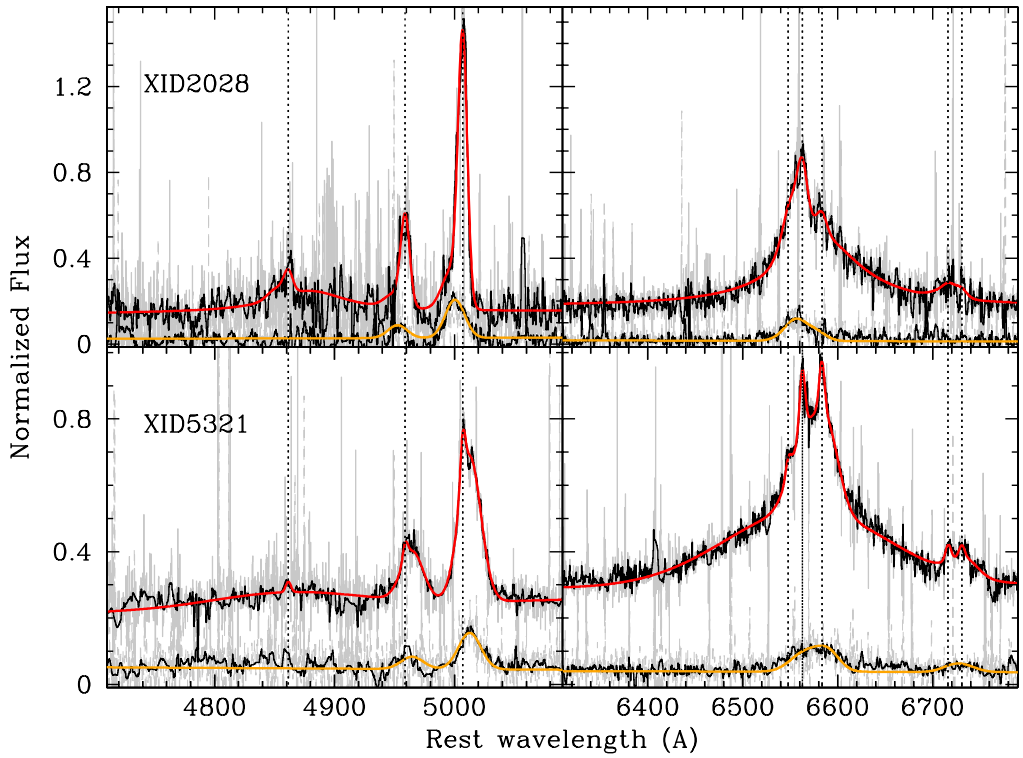

Fig. 6: Spectra of the two quasars normalized so that the intensity of the strongest emission line of the nuclear aperture is unity. For clarity, in the figure the nuclear spectrum of XID2028 is shifted vertically in order to facilitate a visual inspection of the apertures. The grey and black lines indicate the original and the cleaned (of cosmic ray hits, bad pixels and telluric lines) spectra. The red and orange lines indicate the best fit solutions that reproduce the line profiles of the central and the lateral apertures according to the simultaneous fit approach. The dotted lines mark the wavelengths of Hβ, [OIII]λ4959, [OIII]λ5007 (left) and [NII]λ6548, Hα,[NII]λ6581, and the [SII] doublet (right), from left to right, at the systemic velocity.

Cano-Díaz et al. 2012; Harrison et al. 2012, 2014; Westmoquette et al. 2012). We underline that simultaneous fit results, i.e. the first three columns, regard all the emission lines and not only the [OIII]λ5007 emission.

The velocity estimators obtained in the off-nuclear regions have all very high values (e.g., $v_{max} \approx 1530$ km s^{-1} and ≈ 1950 km s^{-1} for XID2028 and XID5321 respectively). Overall, all the velocity estimators are greater in the lateral apertures by up to 45%. Differences between the velocity offsets V_S and the non-parametric ΔV estimators are due to the fact that ΔV depends strongly on the relative flux contributions of different components of the line profile.

4. Additional evidences of outflow

4.1. [OII] emission lines

Zakamska & Greene (2014) found that [OII]$\lambda\lambda$3726,3729 also show outflow signatures, in some cases consistent with extremely broad features as seen in [OIII]. At the redshift of our targets, the [OII] lines are redshifted in the 9200-9600 Å range, sampled by the VIS arm of the X-shooter spectra.

The rest frame wavelengths are inferred by the systemic redshifts obtained in the NIR spectrum (B14). A possible shift between the two different arms of X-shooter instrument could affect the rest frame wavelengths by ~ 10 km s^{-1} (see B14 Section 4.1). The [OII] emission lines were fit with the non-parametric approach described previously, and the results are collected in Table 2. Given the lower S/N of [OII] with respect to the previously analyzed lines, and that the wavelength separation between the doublet lines is comparable with the resolution, in the fits we have assumed a 1:1 flux ratio within the [OII] doublet and the emission lines were treated as a single Gaussian profile.

The [OII] emission lines of XID2028 are at the edge of the spectral range covered by the VIS arm, where the total transmission is very low. For this reason, we reanalyzed the available Keck/DEIMOS spectrum (presented in Fig. 13, B10). The Keck spectrum of XID2028, obtained with DEIMOS (in MOS mode) at Keck-II telescope (Faber et al. 2003) on 2008 January 8, with mildly lower resolution (2.5Å; seeing $\sim$ 1”), was flux-recalibrated in order to renormalize it to the X-shooter spectra by multiplying the spectrum by a constant factor. The best fit solutions are shown in Figure 8: two Gaussian lines, one of them blueshifted with respect to the systemic velocity, are required to reproduce the shape of the emission line. As mentioned above, we have not tried to deblend the doublet, but a hint of the peaks could be in the vicinity of the dashed vertical lines. The [OII] velocity offset of XID2028 is lower ($\sim$30%) than the [OIII] one, but still statistically significant, and support the presence of outflowing ionizing gas also in this lower (but comparable to the [SII]) ionization phase.

As for the NIR, we extracted the XID5321 VIS spectra from the same three regions along the slit. The [OII] emission lines of

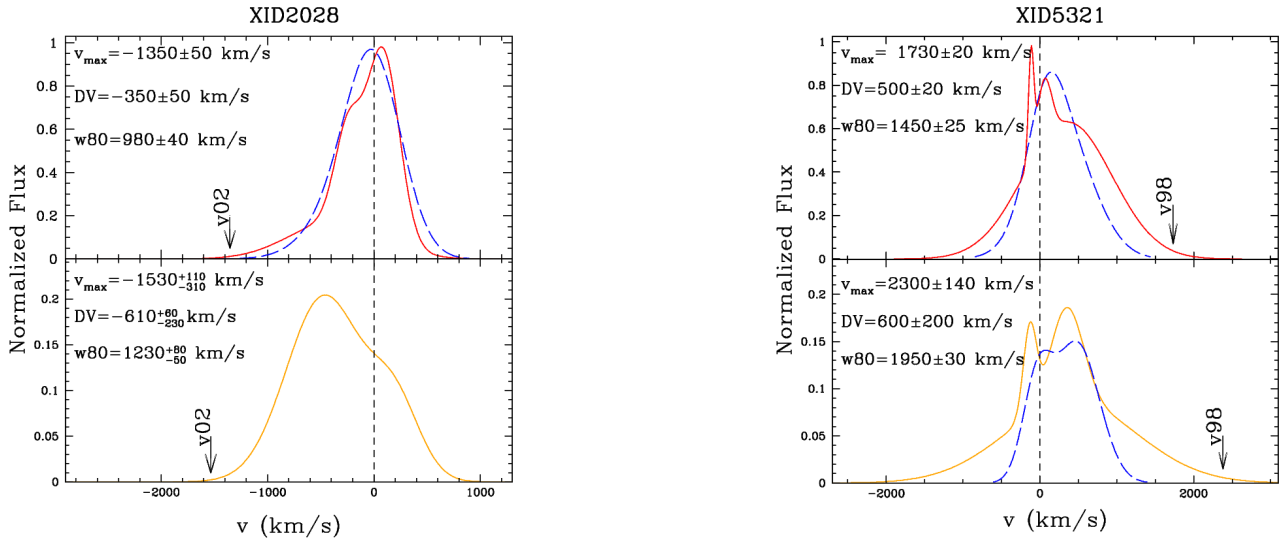

Fig. 7: Comparison between [OIII]λ5007 velocity profiles: red curves for the nuclear apertures in the upper panels, orange curves for the off-nuclear apertures retaining the outflow emission in the lower panel. The non parametric measurements of the [OIII] fit are labeled. We also overplot in long-dashed blue the results for [OII] emission lines fit (see Section 4.1). The [OII] profiles are renormalized in order to facilitate a comparison with the [OIII]. The dashed lines mark the positions chosen as zero velocity (the systemics for [OIII], and the mean wavelength of the [OII] doublet), the arrows mark the 98th and 2th percentiles indicating the v_{max} velocities.

Table 2: Velocity measurements

		$FWHM_{NLR}$	$FWHM_{out}$	V_S	ΔV	v_{max}	$w80$
		(km s^{-1})					
XID 5321							
[*OIII*]	a	-	-	-	-	-	-
[*OII*]		-	-	-	256 ± 15	950 ± 70	1040 ± 55
[*OIII*]	b	310 ± 15	1320 ± 10	350 ± 10	500 ± 20	1730 ± 20	1450 ± 25
[*OII*]		-	-	-	280 ± 20	1050 ± 25	1060^{+60}_{-20}
[*OIII*]	c	-	1650 ± 50	330 ± 20	600 ± 200	1950 ± 30	2300 ± 140
[*OII*]		-	-	-	225 ± 65	1350^{+110}_{-60}	1230^{+200}_{-100}
XID 2028							
[*OIII*]	a	-	1300 ± 45	−385 ± 15	-610^{+60}_{-230}	-1530^{+110}_{-310}	1230^{+80}_{-50}
[*OIII*]	b	510 ± 13	1310 ± 65	−340 ± 30	−350 ± 50	−1350 ± 50	980 ± 40
[*OIII*]	c	-	-	-	-	-	-
[*OII*]	Keck	-	-	-	−100 ± 15	810 ± 20	−900 ± 100

Notes. The values in the first three columns, corresponding to the simultaneous fit results, regard all the emission lines and not only the [OIII] emission. $FWHM_{NLR}$ and $FWHM_{out}$ refer to NLR and outflow components described in Section 3.2.1.

XID5321 are detected in all the three apertures (see Figure 9), and therefore show a greater spatial extension with respect to the [OIII] emission line. The best fitting models are shown in Figure 9 and include two components for the nuclear (*b*) and off-nuclear (*c*) X-shooter spectra, and one component for the off-nuclear (*a*) spectrum. The wavelengths of the [OII] doublet are indicated with dashed vertical lines; here, again, a hint of peaks is in the vicinity of the systemic [OII] lines. Nevertheless, we stress that the lines were fit with the non-parametric approach, and hence the individual Gaussian profiles shown in the figure (solid and dashed blue curves) do not have direct physical interpretation. Even in this case, the [OII] velocity offsets of XID5321 are lower (∼40%) than the [OIII] one, but still significant.

The comparison between the [OIII]λ5007 and [OII] doublets are shown in Figure 7: [OII] velocity profiles are narrower than [OIII], but also shows almost the same asymmetries and shifts, in agreement with the results of Zakamska & Greene (2014).

Summarizing, although at lower S/N, these emission lines confirm the presence of outflowing gas in both targets, and in one case (XID5321) with a greater spatial extension than in the [OIII] emission.

4.2. Absorption Lines

Kpc-scale outflows are observed in both the neutral and ionized gas phases (e.g., Rupke & Veilleux 2011, 2013). The sodium NaD$\lambda\lambda$5890,5896, magnesium MgII$\lambda\lambda$2796,2803 and MgIλ2853 absorption lines are detected in our spectra. Figure 10 shows the Keck/DEIMOS spectrum of XID2028 (on the right) and the X-shooter NIR spectrum of XID5321 (on the left) with the magnesium absorption lines labeled. The Keck spectrum was preferred to the X-shooter one due to its higher S/N. Given the low S/N only the central aperture of XID5321 has been analyzed.

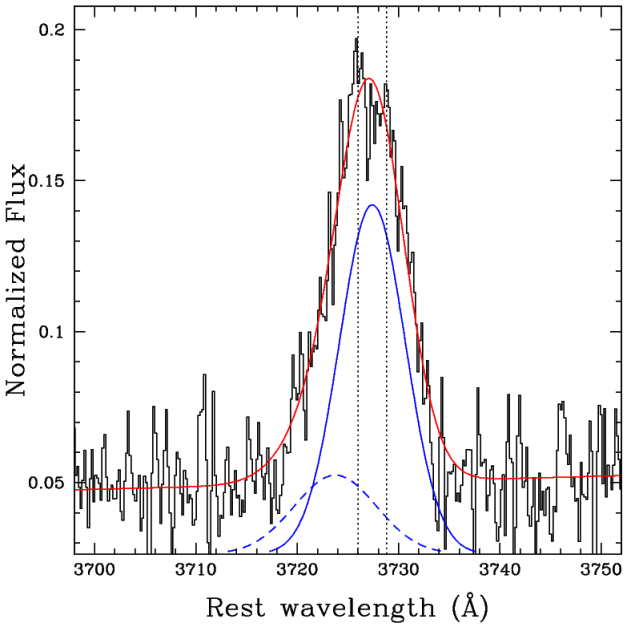

Fig. 8: Keck/DEIMOS spectrum around the [OII]$\lambda\lambda$3726,3729 region of XID2028. The spectrum is normalized so that the intensity of the strongest emission line (in the VIS+NIR wavelength range) of the nuclear aperture is unity. Superimposed on the spectrum are the best fit non-parametric analysis components (solid and dashed blue curves, with arbitrary normalization in order to ease the visualization). The red solid curves represent the sum of all components, including the power-law. Dotted lines mark the wavelengths of the [OII] emission lines.

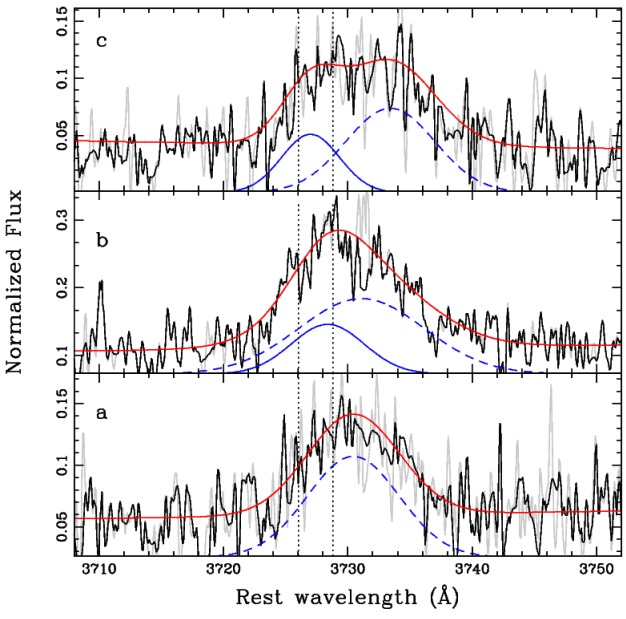

Fig. 9: X-shooter spectra around the [OII]$\lambda\lambda$3726,3729 region of XID5321. Grey and black lines indicate the original and the cleaned (as above) spectra. All the regions (a, b, c) are shown. See previous figure for description.

Each of the magnesium absorption lines of XID2028 were fit with one set of Gaussian profiles, as shown in Figure 10 (left). A velocity shift $V_S \approx$ -330 km s^{-1} with respect to the systemic velocity was found. The sodium profiles, although affected by numerous sky features, seem to be reproduced with the same velocity component of the magnesium profiles.

Each of the magnesium lines of XID5321 were fit with one Gaussian component too, as shown in Figure 10 (right). The corresponding velocity shift is $V_S \approx 260$ km s^{-1}. Even for this source, the sodium profiles were reproduced with the same velocity component of the magnesium profiles.

We stress that for both sources, the sodium regions are strongly affected by sky features; the estimated continua and the Gaussian components did not allow us to study the properties of the absorbing gas, and are presented uniquely as proof of the constrained magnesium components, themselves characterized by low S/N.

The estimated shifts VIS-NIR of a few tens of km s^{-1} between magnesium and sodium lines of XID2028 and XID5321 respectively, are greater than the accuracy of the wavelength calibration ($\sim$ 10 km s^{-1}; $\Delta z = 0.0004$) checked with the position of known sky lines in both VIS and NIR spectra (see B14 Section 4.1). However, given that all our absorption lines suffer of low S/N, they could be fully explained by an imperfect determination of the center of the fitted Gaussian profiles and interpreted as residual error of the (greater) velocity shift V_S values observed.

The XID2028 absorption lines can be ascribed to an outflowing neutral/low-ionization component on the line of sight, with roughly the same velocity shift of the emission lines. The XID5321 absorption lines show a velocity shift of the same magnitude of the emission lines too; possible interpretations are discussed in Section 6.2 and 7.

5. Line ratios

5.1. Estimates of extinction

We used line ratios to estimate the reddening of the sources. This is crucial to derive the corrected [OIII] luminosity used later to estimate the outflow power. We used the Balmer decrements $I(H\alpha)/I(H\beta)$, as measured in our simultaneous fits described in Section 3.1, where I represents the line flux. These can be determined for each set of Gaussian component of the simultaneous fit. In particular, for the nuclear apertures, we used i) the fluxes of the BLR components, ii) the fluxes of the systemic NLR components, iii) the fluxes of the outflow components of the spectra. For the off-nuclear apertures, only one ratio can be estimated. When no Hβ systemic or/and outflow component were detected, we used the standard deviation of the continuum regions (in the vicinity of the emission line) and the FWHM of that set of Gaussian profiles to derive a 3σ upper limit on the flux. Balmer decrements are reported in Table 3.

The $I(H\alpha)/I(H\beta)$ ratio 3.1 (Case B, Gaskell & Ferland 1984) is mostly used to determine the amount of extinction for low-density gas, such as that of the NLR. The average value of BLR Balmer ratio of 3.06 obtained by Dong et al. (2008) for a large, homogeneous sample of $\sim$ 500 low-redshift type 1 AGN with minimal dust extinction effects, suggest that we can assume a ratio of 3.1 also for the BLR. We assumed the same ratio also for the outflow components. Therefore, assuming Case B ratio of 3.1 and the SMC dust-reddening law, the relation between the emission line color excess and the Balmer decrements gives us, for XID2028, a V-band extinction A_V in the range 0.1-1.8, where the first value is evaluated for the NLR component and 1.8 for the outflow component. For XID5321, we obtain an extinction A_V in the range 0.5-1.9, where the first value is a lower limit evaluated

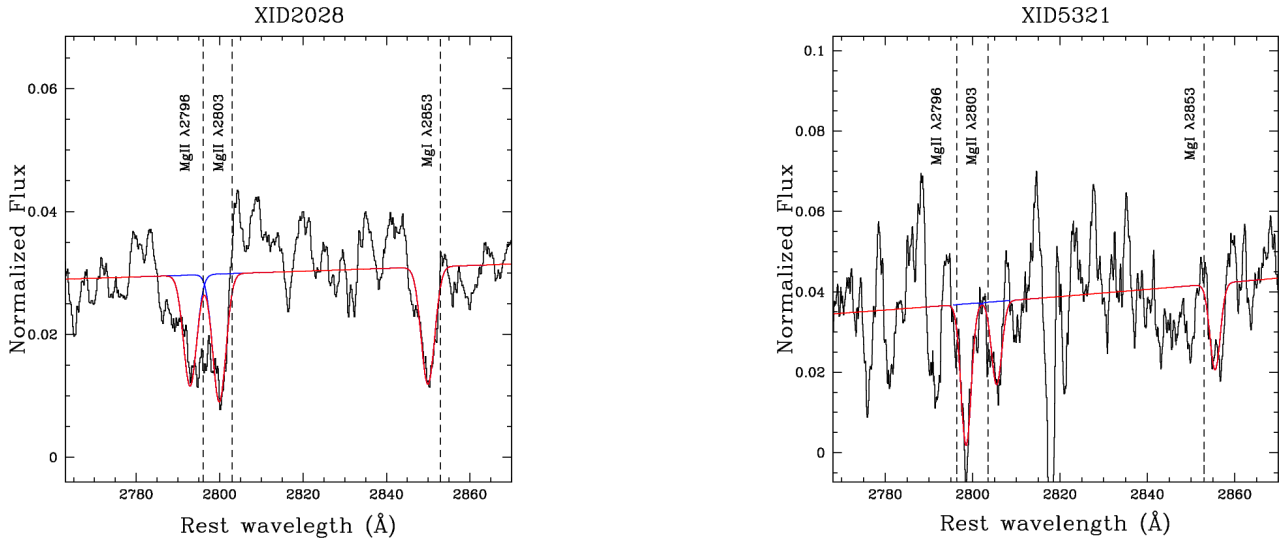

Fig. 10: XID2028 smoothed Keck/DEIMOS spectrum (left) and XID5321 smoothed X-shooter spectrum (right) with the magnesium absorption lines marked. The dashed lines in the spectra mark the rest-frame wavelengths of MgII and MgI, as determined from the systemic redshift. Superimposed on the spectra are the best fit components indicated as solid blue Gaussian curves. The red solid curves represent the sum of the Gaussian components.

Table 3: Balmer decrements

	BLR		NLR		outflow	
	$I(H\alpha)/I(H\beta)$	A_V[a]	$I(H\alpha)/I(H\beta)$	A_V	$I(H\alpha)/I(H\beta)$	A_V
XID 2028						
nuclear (b)	4.4 ± 0.3	0.9 ± 0.4	3.2 ± 0.6	0.1 ± 1.1	6.2 ± 0.5	1.8 ± 0.5
off-nuclear (a)	-	-	-	-	> 1.7	-
XID 5321						
nuclear (b)	6.4 ± 0.5	1.9 ± 0.5	> 3.8	> 0.6	> 3.7	> 0.5
off-nuclear (c)	-	-	-	-	> 1	-

[a] Assuming Case B ratio of 3.1 and SMC extinction curve.

for the outflow component, and 1.9 is obtained for the BLR region. Ratios from the off-nuclear apertures are smaller than 3.1, and no A_V can be derived. Lower limits on the extinction follow from the use of upper limits on the flux of undetected Hβ emission lines. In the following we will use the outflow component Balmer ratios to determine the extinction of the [OIII] outflowing flux. In fact, those obtained in the SED fitting procedure are related to the continuum (BBB) flux that, being affected by a degeneracy between host and AGN accretion disk emission, are significantly more uncertain.

5.2. Rest-frame optical AGN-SF diagnostics

We used the optical diagnostic Baldwin-Phillips-Terlevich diagram (BPT; Baldwin et al. 1981) as a tool to investigate the nature of the ionizing sources. Figure 11 shows the BPT with the results from our spectroscopic analysis. The line drawn in the diagram corresponds to the theoretical redshift-dependent curve used to separate purely SF galaxies from galaxies containing AGN at z=1.5 (Eq. 1 of Kewley et al. 2013). For both sources, all the systemic and the outflow components observed in the different apertures are consistent with an AGN classification.

We tested other possible line ratio diagnostics (e.g., Kewley et al. 2006; Ho 2005), involving [OIII]/[OII] and [OI]λ6300/Hα (detected only in the nuclear spectrum of XID5321). All of them agree with an AGN photoionization origin. We can consequently conclude that, even if present, a star forming origin would play a minor role (similar conclusions have been reached in Rodríguez-Zaurín et al. (2013)).

6. Quantifying the outflow energetics

Quantifying outflow energetics require estimating the kinetic power (P_K) and mass-flow rate ($\dot{M}$) of the outflows. These quantities can be computed when we are able to estimate the temperature, the electron density n_e, the involved emitting luminosity, the spatial scale, i.e. the distance R of the outflowing material from the central source, the outflow velocity, and to infer the geometry distribution. In addition, all the gas components should be probed.

6.1. Ionized component

Following the arguments presented in Cano-Díaz et al. (2012), the kinetic power associated with the ionized component of the outflow can be given by:

$$P_K^{ion} = 5.17 \cdot 10^{43} \frac{C L_{44}([OIII]) v_{0,3}^3}{n_{e3} R_{kpc} 10^{[O/H]}} erg\ s^{-1}, \quad (1)$$

where $L_{44}([OIII])$ is the [OIII] luminosity associated to the outflow component in units of 10^{44} erg s^{-1} and corrected for

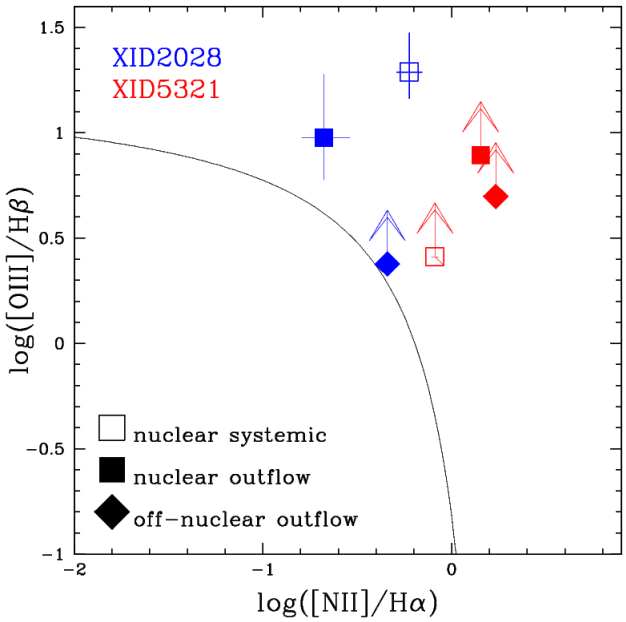

Fig. 11: Standard diagnostic diagram showing the classification scheme by Kewley et al. (2013). The line drawn in the diagram corresponds to the theoretical redshift-dependent curve used to separate purely SF galaxies from galaxies containing AGN (Kewley et al. 2013). Empty and filled squares correspond to the systemic and outflow components of the nuclear aperture; filled diamonds correspond to the outflow components of the off-nuclear apertures. Blue and red points represents XID2028 and XID5321 respectively. Upper arrows represent lower limits, due to undetected Hβ emission lines.

the extinction, n_{e3} is the electron density in units of 1000 cm^{-3}, $v_{0,3}$ is the outflow velocity v_0 in unit of 1000 km s^{-1}, C is the condensation factor (≈ 1), $10^{[O/H]}$ is the metallicity in solar units, R_{kpc} is the radius of the outflowing region in units of kpc.

Our slit-resolved spectroscopy analysis has shown that significant signal in the [OIII] shifted components can be detected out to a projected distance of R $\approx$ 11 kpc (see Figure 5). Therefore we assume the outflow extending out to that radius from the central black hole for both sources (see also Cresci et al. 2014).

Estimates of the electron density of the outflowing gas from the flux ratios of the outflow components in the nuclear apertures of the [SII] doublets can be obtained (Osterbrock 1989): $n_e \approx 2000 - 3000$ cm^{-3} (B14). Although these values are higher than other values routinely used in Eq. 1 (e.g., Liu et al. 2013; Harrison et al. 2014), they are still comparable with other assumptions adopted in low-z AGN/ULIRGs systems (e.g., Rodríguez-Zaurín et al. (2013); Villar-Martín et al. (2014) and references therein). However, these n_e estimates are somewhat ambiguous, given the complexity of the spectral profiles. Moreover, when systemic components are also present, the fitting procedure may produce strongly degenerate results. For these reasons, we use the value obtained from the fit to the [SII] doublet in the off-nuclear aperture (c) of XID5321, $n_e = 120$ cm^{-3}. This electron density, close to the commonly used in similar studies, is adopted for both targets (unfortunately, the off-nuclear (a) aperture of XID2028 did not permit a similar estimate).

Estimates of the metallicity, using the indicators $N2 = [NII]\lambda 6583/H\alpha$ (Pettini & Pagel 2004) and $R23 = ([OII]\lambda\lambda 3726,3728 + [OIII]\lambda\lambda 4959,5007)/H\beta$ (e.g., Pilyugin 2001; Yin et al. 2007), based on the assumption of a stellar ionizing radiation field, are not useful because a large contribution from the AGN is present for both sources. For this reason, we assume a solar metallicity. In fact, even assuming that the outflows reside in metal-rich regions with $9.0 < 12 + log(O/H) < 9.3$ (Kewley et al. 2013; Du et al. 2014), the metallicity would be at most a factor of 2 greater. This is negligible with respect to other sources of uncertainties (see below).

From the extinctions obtained previously from Balmer decrements of outflow components, we obtain values of $A_5007Å \approx 1.8$ and 0.5 (lower limit), corresponding to correction factors of ≈ 6 and 2 for the [OIII] luminosities of XID2028 and XID5321, respectively.

Finally, following Cano-Díaz et al. (2012) and Cresci et al. (2014), we assume that the maximum velocity observed v_{max} is indicative of the outflowing velocity of the gas, while lower velocities are due to projection effects.

Using the values previously indicated and the measured v_{max}, we obtain

$$P_k^{ion}(2028) \approx 4 \cdot 10^{43} erg/s,$$

$$P_k^{ion}(5321) \approx 6 \cdot 10^{43} erg/s,$$

adding the contributions determined in the apertures $(a)+(b)$ and $(b)+(c)$ for XID2028 and XID5321. Namely, for each object, we compute the relative kinetic power adding the corresponding flux measured in the outflow components, and using the maximum v_{max} value (see Table 2). Consequently, using the same assumptions as above and Eq. B8 of Cano-Díaz et al. (2012), we obtain the corresponding outflow mass rates $\dot{M}_{out}^{ion}(2028) \approx 55\ M_\odot\ yr^{-1}$ and $\dot{M}_{out}^{ion}(5321) \approx 50\ M_\odot\ yr^{-1}$.

Equation 1 and Eq. B.8 of Cano-Díaz et al. (2012) assume a simplified model where the wind occurs in a conical region composed of ionized clouds uniformly distributed, under the assumption that most of the oxygen is in the O^{+2} form. Because of this assumption, these values are lower limits for the kinetic power and mass rate of the ionized component.

A confirmation that the estimates from [OIII] are lower limits, comes from the outflow mass ratio computed comparing the [OIII] ionized mass with the Hβ mass estimate, using the measured electron density and assuming an electron temperature $T_e = 2 \cdot 10^4$ K (Osterbrock 1989; Cano-Díaz et al. 2012): $M_{[OIII]}/M_{H\beta} = 0.008\ L_{[OIII]}/L_{H\beta}$. If we assume the same kinematic and extension for Hβ and oxygen emission lines, the corresponding outflow mass rate ratio preserves the same dependency: $\dot{M}_{[OIII]}/\dot{M}_{H\beta} = 0.008\ L_{[OIII]}/L_{H\beta}$. The same applies to the kinetic power ratio.
XID2028 measured luminosity ratio $L_{[OIII]}/L_{H\beta} \approx 10$ in the nuclear region (i.e., where outflowing Hβ is detected), implies that we are underestimating the ionized mass rate by a factor of ≈ 10. XID5321 upper limit on the flux of undetected outflowing Hβ emission line in the nuclear region (see Section 5.1) implies at most a factor of ≈ 20 larger ionized mass rate. As a conservative order of magnitude estimates of the ionized kinetic power and mass rate of the targets we will refer, in the following, to the values previously evaluated, multiplied by 10, in order to account for the $L_{[OIII]}/L_{H\beta}$ ratios. Therefore, our inferred mass rates are $\dot{M}_{out}^{ion}(2028) \approx 550\ M_\odot\ yr^{-1}$ and $\dot{M}_{out}^{ion}(5321) \approx 500\ M_\odot\ yr^{-1}$, and the corresponding kinetic powers are $P_k^{ion}(2028) \approx 4 \cdot 10^{44} erg/s$ and $P_k^{ion}(5321) \approx 6 \cdot 10^{44} erg/s$. For XID2028, these results are

consistent with those obtained from SINFONI near infrared integral field spectroscopy observations: Cresci et al. (2014) estimate from the Hβ flux an outflow mass rate $> 300\ M_\odot\ yr^{-1}$, without extinction correction.

We also derive estimates of the mass rate in more extreme conditions, assuming an electron temperature $T_e = 5 \cdot 10^4$ K, a rescaled electron density ($n_e = 10^2 \cdot T^{0.5} \cdot (r - 1.49)/(5.62 - 12.8r)$, with $r = I([SII]\lambda6717)/I([SII]\lambda6731)$; Acker & Jaschek 1995), and $\dot{M}_{[OIII]}/\dot{M}_{H\beta}$ relation. These conditions are chosen in order to obtain the lowest values of mass rate and $\dot{M}_{[OIII]}/\dot{M}_{H\beta}$ correction factor. We obtain $\dot{M}^{ion}_{out} \approx 100\ M_\odot\ yr^{-1}$, for both the sources. This value, therefore, could be taken as a very conservative lower limit of the total ionized outflow mass rate.

6.1.1. Kinetic power v_0 estimators

Usually, kinetic powers are determined taking as v_0 the velocity offset (defined as the offset between the Gaussian components of the fitting procedure as well as the non-parametric one, i.e. as ΔV as well as V_S; see, e.g., Harrison et al. 2012 and references therein). However, these are projected velocities and therefore may be not representative of the true outflow velocities. Harrison et al. (2012), found that $FWHM_{out}/V_S \approx 2$ for two of their sources showing clear BLR components and, assuming that the outflow could be primarily oriented towards us for this kind of sources, suggest that FWHM$_{out}$/2 may be an adequate approximation of v_0 for other sources. However, we did not find the same ratios (the same conclusions are found for the non-parametric $w80/\Delta V$ ratios), suggesting a different geometry.

We also note that estimates of kinetic power through $w80$ value could be similarly arguable: our $w80$ values are lower in the nuclear region than in the off-nuclear ones. This has possibly significant implications: $w80$ may be not reliable when there is a unique extracted spectrum instead of slit-resolved spectroscopy on different apertures, because the line flux of the systemic component in the core is dominating the emission. At larger radii this should not apply, because the NLR flux is almost suppressed. Therefore, $w80$ values greater in the external regions may be not interpreted as accelerating outflows.

We define the line width $w40$, as the velocity width $v50 - v10$ that contains 40% of the emission flux of the line profile of XID2028, with blueshifted outflow, and as the width $v90 - v50$ of the line profile of XID5321, with redshifted outflow signatures (Cresci et al. 2014). These estimators, regarding only the emission of more certain outflowing gas origin, can be useful to quantify possible outflow velocity variations between the different regions. XID2028 shows a roughly constant value ($w40 = 580 \pm 30$ and 610 ± 40 km s^{-1} for the off-nuclear (a) and nuclear (b) regions respectively), and this may indicate that the outflow is not accelerating. This is not the case for XID5321, where $w40$ shows a significant variation between the two regions ($w40 = 1730 \pm 20$ and 2380 ± 200 km s^{-1} for the nuclear (b) and off-nuclear (c) apertures), mostly attributable to $v90$ changes. In this source, therefore, an accelerating outflow could be present.

All these arguments suggest that the kinetic powers evaluated both in this study and in others using similar velocity estimators, should be considered only order of magnitude estimates. To give a better feeling of the uncertainties, for these two sources, v_{max} and $w80$ are in reasonable agreement (within $10 - 30\%$), but $\Delta V \sim 0.3 v_{max}$ implies a variation of a factor of ~ 40 in kinetic power estimates. Improved observational constraints are needed to test kinematic models of these outflows, and allow better estimation of kinetic energy and mass rates.

6.2. Neutral component

In the optical thin approach, from the ratio of the Equivalent Width (EW) for any two transitions of the same ion it is possible to estimate the ion integrated column density. Namely, the EW doublet ratio can assume values in the range 2-1, corresponding to optical depth in the range $0, +\infty$ (Bechtold 2003).

The measured EW ratio of MgII$\lambda\lambda$2796,2803 of XID5321 is 1.7, therefore the magnesium column density can be inferred from the EW of MgIIλ2796 (see Bechtold 2003 for more details). Following the arguments presented in Bordoloi et al. (2013), i.e. assuming no ionization correction ($N_{Mg} = N_{MgII}$), no correction for saturation, and a solar abundance of Mg with a factor of -1.3 dex of Mg depletion onto dust, we obtain a hydrogen column density $N_H(5321) = 3 \cdot 10^{19}$ cm^{-2}.

The measured EW of the magnesium lines of XID2028 are instead consistent with a doublet ratio of ~ 1, corresponding to a high optical depth. In this case, the absorption lines would be approaching the flat part of the curve of growth and their column density cannot be inferred from their EW. We estimate an apparent optical depth and a conservative lower limit of the hydrogen column density, $N_H(2028) > 9 \cdot 10^{19}$cm^{-2}, following the method used by Bordoloi et al. (2013) and using the same assumptions as above.

For both sources, we have used the EW of low ionization MgII to estimate lower limit of neutral hydrogen column densities, instead of NaD because of the difficulties inherent the sodium fits (see Section 4.2). This corresponds to assume these absorption lines as in a unique absorbing system. The assumption is justified by the fact that all the absorption lines seem to have same kinematics. Moreover, given that they have roughly the same velocity shift of the outflowing ionized gas, we assume that this absorbing system has the same kinematic and extension of the ionized one, i.e. that neutral and ionized components are closely connected (see also discussion below).

Corresponding neutral mass outflow rates can be estimated from Eqs. 7-8 of Weiner et al. (2009),

$$\dot{M}^{H}_{out} \simeq 7 \cdot \left(\frac{N_H}{10^{20} cm^{-2}}\right)\left(\frac{R}{5kpc}\right)\left(\frac{v_0}{300 kms^{-1}}\right) M_\odot\ yr^{-1}, \quad (2)$$

assuming a flow that extends from radius 0 to R.

For the assumptions discussed above, using the maximum v_{max} value and the maximum extension observed for the [OIII] emission lines, we obtain mass outflow rate $\dot{M}^{H}_{out}(2028) > 80\ M_\odot\ yr^{-1}$ and $\dot{M}^{H}_{out}(5321) > 35\ M_\odot\ yr^{-1}$. Given the adopted assumptions, these results represent lower limits. Adding the previous results (ionized items), we obtain lower limits of the total ionized and neutral mass outflow rate: $\dot{M}^{tot}_{out}(2028) > 630\ M_\odot\ yr^{-1}$ and $\dot{M}^{tot}_{out}(5321) > 535\ M_\odot\ yr^{-1}$.

7. Discussion and conclusions

We analyzed in great detail the optical, NIR and X–ray spectra of two luminous, obscured QSOs, selected from the XMM-COSMOS survey to be in the "blow-out" phase of galaxy-AGN co-evolution. Although not as extreme as other very luminous QSOs selected from all-sky surveys and thought to be caught in this crucial feedback phase (with $L_{bol} > 10^{47-48}$ erg s^{-1}, e.g. the WISE-selected quasars in Weedman et al. 2012; Eisenhardt et al. 2012, or the UKIDSS-selected objects in Banerji et al. 2012, 2014), these two sources are among the most luminous objects at z$\sim$ 1.5 ($L_{bol} > 10^{46}$ erg s^{-1}) of the entire X–ray selected sample in the much smaller area covered by the COSMOS survey,

thus more representative of the entire luminous population. The availability of a complete and deep multiwavelength coverage within the COSMOS field enables a full characterization of the host galaxy and accretion rates properties of these two extreme sources which is not possible, at similar depths, in other targets given the limited follow-up available.

XID2028 and XID5321 are "X–ray loud", as per their selection, based on optically dim counterparts associated to bright X–ray and MIR emissions. In addition, when compared with the average SED of Type 2 AGN with similar bolometric luminosity, the X–ray flux of XID2028 and XID5321 is less absorbed than average (the X–ray slope in Figure 2 is flatter than the Lusso et al. (2011) X–ray SED). Indeed, thanks to the high quality X–ray spectra (> 1500 counts) we were able to robustly constrain the column density in the range $N_H \sim 6 - 7 \times 10^{21}$ cm^{-2}.

Despite the relatively high SFR observed (SFR$\sim$ 250 $M_\odot$ yr^{-1}), the high X–ray luminosity coupled with the low level of column density observed in our two sources, argues against an obscured accretion phase (e.g., in evolutionary models when the SFR is at its peak, it should be associated with high nuclear and host obscuration; see, e.g., Hopkins et al. 2008). The overall properties extracted from the SEDs and the X–ray spectra, instead, definitely point towards a scenario in which the AGN is caught in the subsequent phase where most of the BH mass has been already fully assembled. This is witnessed by the Broad components observed in the Hα region, corresponding to BH masses $M_{BH} \sim 10^{9-10}$ M$\odot$ (Bongiorno et al. 2014). The fairly high accretion rates observed in our two targets ($L_{bol}/L_{Edd} \sim 0.01 - 0.05$) are also in agreement with a scenario in which our targets are caught in the very short blow-out phase (see Fig. 2 of Hopkins et al. 2005), between the obscured and unobscured peaks of bolometric luminosity and accretion rate.

The X-shooter (VIS and NIR) and Keck/DEIMOS spectra allowed us to simultaneously sample different gas components and phases, via spatially resolved spectroscopy of the emission lines complexes (Hβ+[OIII] and Hα+[NII]+[SII] in the NIR spectra, [OII] in the VIS and DEIMOS spectra). In particular, with respect to the analysis presented in B14, in where we discuss only the spectra of these two sources extracted in the nuclear regions, here we investigated the kinematic properties of the gas observed at projected distances of 6-12 kpc. In addition, we studied the absorption properties of the MgI, MgII and NaD systems and we could put better constraints on the properties of the outflows, including their neutral components.

First of all, we found clear evidence for the presence of outflow components in all the emission lines investigated in one of the two off-nuclear apertures we extracted for each source (see Section 3 and Figures 5, 7 and 6). In the hypothesis that these components are tracing outflowing winds, we were therefore able to demonstrate that the outflow has propagated well within the host galaxy (up to 10-12 kpc scale; see Section 3.1). The extension of the outflow region of XID2028 has been confirmed by SINFONI J-band data, where the outflow has been unambiguously resolved and its impact on the host galaxy has been also extensively discussed (Cresci et al. 2014).

In order to constrain at best the velocity of the outflows, we performed both non-parametric analysis and simultaneous fit of the emission lines. The non-parametric measurements of the emission lines removed the degeneracy between the systemic and outflow components, allowing better constraints on the velocity properties (Section 3.2.2), while the simultaneous fitting allowed us to quantify the relative outflow luminosities at different radii and to disentangle the contribution of the outflow fluxes from those of the NLR in the central apertures (Section 3.2.1).

With a solid handling of the most important observational constraints (velocity and spatial scale) needed to derive the outflow kinetic powers and mass outflow rates, and with the additional information we could derive from the absorption systems, we could draw conclusions on their associated energetics and mass outflow rates (see Section 6.2). The kinetic power fiducial values obtained, being greater ($\gtrsim$ 3) than those presented in B14, can only be attributed to AGN-driven outflows and definitely rule out a SF origin for the outflow. In fact, an AGN origin of the outflow, with kinetic powers of $\approx$ 4% of the AGN bolometric luminosity, is in agreement with the prediction by AGN feedback models (e.g., King 2005), and is favored compared to the very high coupling needed between SF and the wind (see the detailed discussion of B14, Sec. 6.1, and references therein). An AGN origin for the observed outflowing winds is also supported by our BPT analysis: all the outflow components observed in the different apertures for both sources lie in the region of AGN photo-ionization (see Figure 11 and Section 5.2).

Moreover, the momentum fluxes, defined as $\dot{P} = \dot{M}_{out} v_0$, inferred for these outflows are $\dot{P}(2028) \approx 6.1 \cdot 10^{36}$ dyne and $\dot{P}(5321) \approx 6.6 \cdot 10^{36}$ dyne. These values are in excess of $\approx$ 10 times the radiative momentum flux from the central black hole, $\dot{P}_{rad} = L_{bol}/c$. This excess is consistent with the "momentum boost", $\dot{P}/\dot{P}_{rad}$, observed in local ULIRGs dominated by AGN and in luminous QSO (Rupke & Veilleux 2011; Sturm et al. 2011; Faucher-Giguère & Quataertet 2012), and required to reproduce the normalization of the relation among BH mass and stellar velocity dispersion, $M_{BH} - \sigma$, in numerical simulations (DeBuhr et al. 2012).

Finally, we obtain the dynamical time $t_d \approx R/v_0$ of the outflow: $t_d(2028) \approx 8 Myr$ and $t_d(5321) \approx 5 Myr$. The dynamical time scales of these outflows are much longer than the recombination time scales of the [OIII] lines (a few tens of yr; e.g., Osterbrock 1989), as also noted by other authors (e.g., Cresci et al. 2014; Greene et al. 2012). Given the spatial extension of the [OIII] emission, we can prove the presence of AGN emission over a period of $t_e \sim 3 \cdot 10^4 yr$. This time estimation comes from the size of the outflow divided by the velocity of light c. In fact, for these two sources, given that the AGN is the main source of O^{+2} ionization, black hole accretion and consequent AGN emission are required. However, we can not discriminate between countinuous and intermittent AGN emission over the entire dynamical time period, if intermittent AGN fueling takes place on time scales much shorter than t_e, or on larger time scales. Moreover, even the outflow could be continuously or intermittently refilled. Higher angular resolution data are required to infer the distributions of the ejected material and to obtain more robust estimates of the outflow properties.

Despite a remarkable set of common properties in the two targets (similar host galaxies and accretion properties, similar broadening of the lines and spatial extension), XID2028 and XID5321 present one striking difference: the outflow component is *blueshifted* in XID2028 (as observed in basically all the objects with broad [OIII] reported in the literature) while in XID5321 the outflow component is *redshifted*. Below we will therefore summarize separately the properties of the two systems we were able to infer from all the available data.

7.1. The blueshifted outflow in XID2028

The interpretation of the data we have for XID2028 is relatively simple. The absorption lines of XID2028, tracing the low ionization/neutral gas, show a blueshift nearly like that observed in the emission lines, with $V_S \sim$ -300 km s^{-1} with respect to

the systemic velocity, easily explained as outflowing gas along the line of sight. The [OII] emission doublet as sampled by the Keck/DEIMOS spectrum (Figure 8) also shows almost the same asymmetries and shifts, within the errors, of [OIII] (Figure 7; see also Zakamska & Greene 2014 for similar [OII] and [OIII] broad profiles observed in SDSS spectra). With respect to the analysis presented in B14 and Cresci et al. (2014) we therefore report, for the first time in this prototypical system, also the presence of an outflow in the lower ionization [OII] emission and in the neutral component.

Under the assumptions discussed in Section 6.2, we obtain a lower limit on the outflow mass rate for the neutral component that, added to the ionized component, gives us a lower limit on the outflow mass rate, $\dot{M}_{out}^{tot}(2028) > 630\ M_{\odot}\ yr^{-1}$, without taking into account the presence of a possible molecular component. We also obtain a kinetic power associated to the outflow of $\sim 4 \cdot 10^{44}$ erg s^{-1}, where, starting from Equation 1 for the ionized kinetic power, we have taken into account a correction factor of 10 from the comparison between the [OIII] and Hβ mass rate estimates in the nuclear region (see Section 6.1). Although obtained through different observational constraints, these results are overall consistent with those presented in Cresci et al. (2014) and unambiguously point towards an AGN origin for the observed wind (see Section 6.1).

7.2. The redshifted outflow in XID5321

For XID5321 the interpretation of the observational constraints we obtained in our analysis (in particular, the redshifted absorption that shows a velocity shift of the same magnitude of the emission lines) is more complex.

The similarity between the velocity shift of absorption and ionized lines suggests that neutral and ionized gas are closely connected: in fact, some of the ionized outflowing gas could become again neutral (e.g., Emonts et al. 2005). In this case, the redshifted absorption lines observed in XID5321 could be explained as outflowing absorbers along the line of sight, illuminated by the light of the host galaxy behind the redshifted outflowing material. Figure 12 shows a cartoon illustrating the extended host galaxy disk (grey area) and our inferred geometry for the bi-conical outflow (blue and red areas) of XID5321. In this scenario, the observed outflow should corresponds to the receding red cone, while the blue cone is obscured by the host galaxy. In addition, the AGN system and the associated torus are warped with respect to the galaxy disk.

An outflowing absorbing medium on the line of sight (indicated with dotted-dashed lines in the figure), in or close to the red cone and illuminated by the light of the extended host galaxy behind, could be responsible for the absorption lines observed, with the same kinematics and extension of the ionized outflowing gas.

The cartoon also helps us to understand the origin of the broad wings observed in the [OIII]λ5007 emission line (Figure 5). A blue wing could be originated by the near-side of the outflow (in the upper part of the figure), where the velocities have negative projected components along the line of sight. For this reason, these velocities are indicated with cyan arrows. The bulk has instead velocities with positive line of sight components (orange arrows) and determines the core of the line profile. An alternative option is that the bi-conical outflow has a more wider opening angle in such a way that the blue wing is originated by the blue cone extended up to the host galaxy. In these possible scenarios, the positive maximum velocity, v_{max}, is indicative of the outflow velocity because it is originated by the gas components at the periphery of the visible cone and closest to the line of sight. All the other gas components have lower velocities because of greater projection effects.

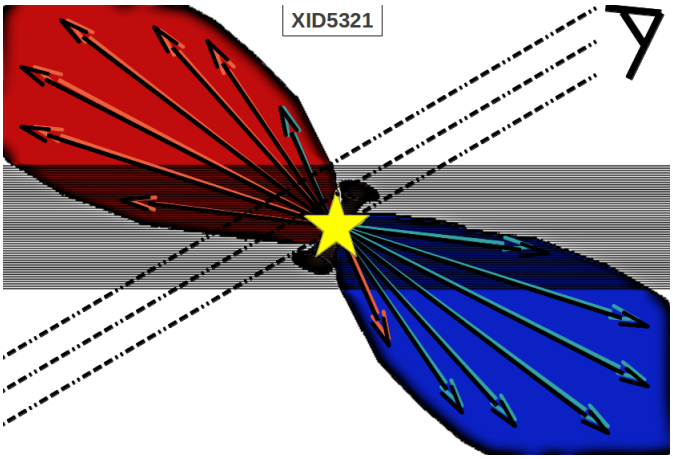

Fig. 12: Schematic cartoon showing the extended host galaxy (grey area) and conical outflow of XID5321 (blue and red areas). The blue and red lobes represents the blueshifted and redshifted gas. The yellow star and the cylindrical shape show the position of the driving center and the torus. The line of sight is indicated.

In addition, the proposed geometry also explains why we see the BLR responsible for the emission of the Broad Hα (i.e., we have an almost unobscured view to the nucleus), why the broad Hβ is heavily extincted (i.e., probably by the galaxy disk; see Table 2), and why we measure a relatively low X–ray column density (i.e., the line of sight does not fully intercept the torus), therefore justifying the type 1.8 of the source.

XID5321 [OII] lines show a great spatial extension, allowing us to study the emission in the three apertures (Figure 9). It turns out that the [OII] profiles tend to be wider and more redshifted from *a* to *c*. A possible explanation is that the low ionization component of the outflow could have a wider opening angle than the highly ionization component.

Following the same arguments mentioned above for XID2028, we obtain a kinetic power associated to the outflow of $\sim 6 \cdot 10^{44}$ erg s^{-1}. Following the scenario presented in Figure 12, a lower limit on the outflow mass rate for the neutral component added to the ionized term was obtained: $\dot{M}_{out}^{tot}(5321) > 535\ M_{\odot}\ yr^{-1}$.

Although the scenario described above seems to fit our diverse constraints and is favored, we should notice that the redshifted systems of XID5321 could in principle also be consistent with the existence of an object approaching the AGN, and/or with a kinematics disturbed by a double nucleus in the galaxy. This second scenario may be suggested by the double peak in the Hα region (see Figure 6): the narrow peak we associate with the [NII]λ6583 could instead be the Hα of a second source blended in the X-shooter spectrum (within 0.8" and therefore within $\sim$ 6 kpc from the brightest AGN). In this case, we should see at least a second shifted [OIII]λ5007 emission line too, at observed wavelengths 1240.5 nm. A closer view of the spectrum presented in Figure 5 does not allow us to exclude the presence of a weak emission line and high resolution imaging with HST will be vital to disentangle the nature of this source (see, e.g., Greene et al. 2012).

7.3. Outlook

The observed extents of the outflows for our two targets, although obtained through NIR integrated spectra, are among the largest reported in the literature for high-z luminous QSOs measured from IFU data. For example, Cano-Díaz et al. (2012) reported clear evidence of outflowing gas on a much smaller scale ($\sim$ 3 kpc, on scale even lower than those sampled by our central apertures). Similarly, Alexander et al. (2010) detected broad and shifted components in J1237 out to 4-8 kpc within the galaxy, on scales comparable to our nuclear apertures. This highlights the power of high resolution slit spectroscopy in unambiguously revealing complex kinematics and assessing the order of magnitude of the energetics of the systems, when applied to luminous QSOs. Larger programs of NIR follow-up of large area and deep fields X–ray selected sources (such as those from XXL and Stripe82) can be exploited to single out the most promising cases.

Differently from our two targets, luminous QSOs detected in large area IR surveys seem to be "X–ray weak": the X–ray weakness can be ascribed to the high column density along the line of sight, as proposed for three WISE-selected QSOs at z$\sim$ 2 (Stern et al. 2014), or possibly to an intrinsically low disk/corona emission, as observed in J1234+0907(Banerji et al. 2014). In order to have a complete picture of the complex interplay between the X–ray luminosity, the X–ray absorption, and the winds properties, it is essential to gather a complete sample of sources with deep optical, NIR and X–ray data over a large luminosity range. A crucial role will be played by follow-up observations with PdBI and ALMA, aimed to detecting the molecular gas components expected to be associated to the outflows. As a first step, we obtained PdBI observations of the CO(3-2) transition in XID2028 with the aim of measuring the gas mass in the system.

Finally, although the results of our study have shown that slit-resolved spectroscopy is more adequate than a single aperture nuclear spectra to put constraints on the properties of the outflows, we have found structural complexities for which integral field spectroscopy is required, especially in the case of XID5321 where possible accelerating outflow, or double nucleus could be present. Moreover, spatially resolved NIR spectroscopy can also be used to probe the impact of outflows on the host galaxy (see, e.g., Cano-Díaz et al. 2012).

Acknowledgments

This work is based on observations made at the European Southern Observatory, Paranal, Chile (ESO program 090.A-0830(A)) and with Keck/DEIMOS, and on observations obtained with XMM-*Newton* and *Herschel*, two ESA Science Missions with instruments and contributions directly funded by ESA Member States and the USA (NASA). MP and MB acknowledge support from the FP7 Career Integration Grant "eEASy" ("SMBH evolution through cosmic time: from current surveys to eROSITA-Euclid AGN Synergies", CIG 321913), and the DFG cluster of excellence "Origin and Structure of the Universe". Support for this publication was provided by the Italian National Institute for Astrophysics (INAF) through PRIN-INAF 2011 ("Black hole growth and AGN feedback through the cosmic time") and by the Italian ministry for school, university and research (MIUR) through PRIN-MIUR 2010-2011 "The dark Universe and the cosmic evolution of baryons: from current surveys to Euclid". We gratefully acknowledge the unique contribution of the entire COSMOS collaboration for making their excellent data products publicly available; more information on the COSMOS survey is available at `http://www.astro.caltech.edu/~cosmos`.

References

Acker A. & Jaschek C., 1995, Sci, 270, 1236J
Baldwin J.A., Phillips M.M., Terlevich R., 1981, PASP, 93, 5
Bae H. & Woo J., 2014, ApJ, arXiv:1409.1580
Banerji M., Fabian A.C., McMahon T.G., 2014, MNRAS, 439, 51
Banerji M., McMahon R.G., Hewett P.C., et al., 2012, MNRAS, 427, 2275B
Bonzini M., Padovani P., Mainieri V., et a., 2013, MNRAS, 436, 3759
Bongiorno A., Maiolino R., Brusa M., et al., 2014, MNRAS, 443, 2077
Bongiorno A., Merloni A., Brusa M., et al., 2012, MNRAS, 427, 3103
Bordoloi R., Lilly S.J., Hardmeier E., et al. 2013, arXiv:1307.6553
Brusa M., Civano F., Comastri A., et al., 2010, ApJ, 716, 348
Brusa M., Bongiorno A., Cresci G., et al., 2014, arXiv:1409.1615
Cano-Díaz, Maiolino R., Marconi A., Netzer H., Shemmer O., Cresci G., 2012, A&A, 537, L8
Cappelluti N., Brusa M., Hasinger G., et al., 2009, A&A, 497, 635
Cicone C., Feruglio C., Maiolino R., et al., 2012, A&A, 543, A99
Cicone C., Maiolino R., Sturm E., et al., 2014, A&A, 562, A21
Cresci G. et al., 2014, in preparation
DeBuhr J., Quataert E., Ma C.P., et al., 2012,MNRAS, 420, 2221
Delvecchio I., Gruppioni C., Pozzi F., et al. 2014, MNRAS, 439, 2736
D'Odorico S., Dekker H., Mazzoleni R., et al., 2006, in Society of Photo-Optical Instrumentation Engineers (SPIE) Conference Series, Vol. 6269, Society of Photo-Optical Instrumentation Engineers (SPIE) Conference Series
Dong X., Wang T., Wang J., et al., 2008, MNRAS, 383,581
Du P., Wang J., Hu C., et al.,2014, MNRAS, 438, 2828D
Elvis M., Wilkes B.J., McDowell J.C., et al. 1994, ApJS, 95, 1
Eisenhardt P.R.M., Wu J., Tsai C.W., et al., 2012, ApJ, 755, 173
Emonts B.H.C., Morganti R., Tadhunter C.N., et al., 2005, MNRAS, 362, 931
Fabian A. C., 2012, ARAA, 50, 455
Faber S.M., Phillips A.C., Kibrick R.I., et al, 2003, SPIE, 4841, 1657F
Faucher-Giguère C.-A. & Quataert E., 2012, MNRAS, 425, 605
Ferrarese L. & Ford H., 2005, SSRv, 116,523
Feruglio C., Maiolino R., Piconcelli E., et al., 2010, A&A, 518, L155
Föerster-Schreiber N.M., Genzel R., Newman S.F., et al., 2014, ApJ, 787, 38
Fu H., Yan L., Myers A. D., Stockton A., Djorgovski S.G., Aldering G., Rich J. A., 2012, ApJ, 745, 67
Gandhi P., Horst H., Smette A., et al, 2009, A&A, 502, 457
Gaskell C.M., Ferland G. J., 1984, PASP, 96, 393
Genzel R., Föerster-Schreiber N.M., Rosario D., et al., 2014, arXiv 1406.0183
Glikman E., Helfand D.J., & White R.L. 2006, ApJ, 640, 579
Greene J. E., Zakamska N. L., Smith P. S., 2012, ApJ, 746, 86
Harrison C.M., Alexander D.M., Mullaney J.R., et al., 2014, MNRAS, 441, 3306H
Harrison C.M., Alexander D.M., Swinbank A.M., et al., 2012, MNRAS, 426, 1073
Hasinger G., Cappelluti N., Brunner H., et al., 2007, ApJS, 172,29
Heckman T.M., Armus L., Miley G.K., 1990, ApJS, 74, 833
Ho, L. C. 2005, ApJ, 629, 680
Hopkins P. F., Hernquist L., Cox T. J., Keres D., 2008, ApJS, 175, 356
Hopkins P.F., Hernquist L., Cox T.J., Di Matteo T., Robertson B., Springel V., 2006, ApJS, 163, 1
Hopkins P.F., Hernquist L., Martini P., et al., 2005, ApJL, 625, L71
Ivison R.J., Swinbank A.M., Swinyard B., et al., 2010, A&A, 518, L31
James, F. & Roos, M. 1975, Computer Phys. Comm., 10, 343
Kewley L.J., Maier C., Yabe K., et al., 2013, ApJ, 774, L10
Kewley L. J., Groves B., Kauffmann G., Heckman T., 2006, MNRAS, 372, 961
King A., 2005, ApJL, 635, L121
Kormendy J. & Ho L.C., 2013, ARAA, 51, 511
Lapi, A., Raimundo, S., Aversa, R., et al. 2014, ApJ, 782, 69
Lanzuisi G., Ranalli P., Georgantopoulos I., et al., 2014, A&A, arXiv:1409.1867

Liu G., Zakamska N. L., Greene J. E., Nesvadba N., Liu X., 2013b, MNRAS, 436, 2576
Liu X., Shen Y., Strauss M.A., Greene J.E., 2010, ApJ, 708, 427
Lusso E., Hennawi J.F., Comastri A., et al., 2013, ApJ, 777, 86
Lusso E., Comastri A., Simmons B.D., et al., 2012, MNRAS, 425, 623L
Lusso E., Comastri A., Vignali C., et al., 2011, A&A, 534, A110
Lutz D., Poglitsch A., Altieri B., et al., 2011, A&A, 532, A90
Magorrian J., Tremaine S., Richstone D., et al., 1998, AJ, 115, 2285
Mainieri V., Bongiorno A., Merloni A., et al., 2011, A&A, 535, A80
Maiolino R., Marconi A., Salvati M., Risaliti G., Severgnini P., Oliva E., La Franca F., Vanzi L., 2001, A&A, 365, 28
Maiolino, R., Gallerani, S., Neri, R., et al. 2012, MNRAS, 425,L66
Marconi A. & Hunt L.K., 2003, ApJ, 589, L21
Menci N., Fiore F., Puccetti S., Cavaliere A., 2008, ApJ, 686, 219
Bechtold J., 2003, "Quasar absorption line" in Galaxies at high redshift, Eds. Pérez-Fournon I., Balcells M., Moreno-Insertis F., & Sánchez F., (Cambridge: Cambridge U. Press)
Pettini M. & Pagel B.E.J., 2004, MNRAS, 348, L59
Pilyugin, L. S. 2001, A&A, 374, 412
Prevot M.L., Lequeux J., Prevot L., et al., 1984, A&A, 132,389
Osterbrock D.E., 1989, Astrophysics of Gaseous Nebulae and Active Galactic Nuclei. University Science Books, Mill Valley, CA
Raimundo S.I., Fabian A.C., Bauer F.E., et al., 2010, MNRAS, 408, 1714
Rodighiero G., Daddi E., Baronchelli I., et al., 2011, ApJ, 739, 40
Rodríguez-Zaurín J., Tadhunter C.N., Rose M., Holt J., 2013, MNRAS, 432, 138
Rupke D.S.N. & Veilleux S., 2013, ApJ, 768, 75
Rupke D.S.N. & Veilleux S., 2011, ApJ, 729, L27
Schinnerer E., Sargent M.T., Bondi M., et al., 2010, ApJS, 188, 384
Scoville N., Aussel H., Brusa M., et al., 2007, ApJS, 172, 1
Spergel D.N., Verde L., Peiris H.V., et al., 2003, ApJS, 148, 175
Sturm E., González-Alfonso E., Veilleux S., et al., 2011, ApJ, 733, L16
Veilleux S., Cecil G., Bland-Hawthorn J., 2005, ARAA, 43, 769
Vernet J., Dekker H., D'Odorico S., et al., 2011, A&A, 536, A105
Villar-Martín M., Humphrey A., Delgrado R.G., et al., 2011, MNRAS 418, 2032
Villar-Martín M., Emonts B., Humphrey A., et al., 2014, MNRAS, 440,3202
Weedman D., Sargsyan L., Lebouteiller V., at al.,2012, ApJ, 761, 184
Weiner B.J., Coil A.L., Prochaska J.X., et al., 2009, ApJ, 692, 187
Westmoquette M.S., Clements D.L., Bendo G.J. and Khan S.A., 2012, MNRAS, 3173
Whitaker, K. E., van Dokkum, P. G., Brammer G., Franx, M., 2012, ApJ, 754, 29
Yin, S. Y., Liang, Y. C., & Zhang, B. 2007, ASPC, 373, 686
Zakamska N.L. & Greene J.E., 2014, MNRAS, 442, 784
Zubovas K. & King A.R., 2012, ASPC, 460, 235